

Improving relativistic energy density functionals with tensor couplings

Stefan Typel^{1,2,3*} and Shalom Shlomo⁴

^{1*}Technische Universität Darmstadt, Fachbereich Physik, Institut für Kernphysik,
Schlossgartenstraße 9, Darmstadt, 64289, Germany.

²GSI Helmholtzzentrum für Schwerionenforschung, Theorie, Planckstraße 1,
Darmstadt, 64291, Germany.

³Helmholtz Forschungsakademie Hessen für FAIR (HFHF), GSI Helmholtzzentrum
für Schwerionenforschung, Campus Darmstadt, Schlossgartenstraße 2, Darmstadt,
64289, Germany.

⁴Texas A&M University, Cyclotron Institute, College Station, 77843, Texas, USA.

*Corresponding author(s). E-mail(s): stypel@ikp.tu-darmstadt.de;
Contributing authors: s-shlomo@tamu.edu;

Abstract

Energy density functionals (EDFs) have been used extensively with great success to calculate properties of nuclei and to predict the equation of state (EOS) of dense nuclear matter. Besides non-relativistic EDFs, mostly of the Skyrme or Gogny type, relativistic EDFs of different types are in widespread use. In these latter approaches, the effective in-medium interaction is described by an exchange of mesons between nucleons. In most cases, only minimal meson-nucleon couplings are considered. The effects of additional tensor couplings were rarely investigated. In this work, a new relativistic EDF with tensor couplings and density dependent minimal meson-nucleon couplings will be presented. The parameters of the model are determined using a carefully selected set of experimental data with realistic uncertainties that are determined self-consistently. Predictions for various nuclear observables, the nuclear matter equation of state, and properties of neutron stars are discussed.

Keywords: Relativistic energy density functional, tensor couplings, parameterisation, nuclear properties, nuclear matter, equation of state, neutron stars

1 Introduction

For more than half a century, energy density functionals (EDFs) have been used with great success in the description of atomic nuclei across the nuclear chart and nuclear matter over a large range of densities and isospin asymmetries. Many improvements were introduced in these phenomenological models leading to a more and more precise prediction of nuclear observables but, nevertheless, the

quest for further improvements remains. There are different strategies to develop more accurate EDFs. They either follow a systematic approach, e.g., using expansions in power of small quantities, or try to incorporate known effects in a more heuristic way.

EDFs exist in different versions. Most well known are non-relativistic approaches that employ convenient representations of effective in-medium interactions between nucleons, e.g., the Skyrme or Gogny type models [1–4]. Relativistic or covariant EDFs start from a field-theoretic approach where the interaction is described by meson-exchange taking medium dependent effects into account in different ways [5–15]. Either self-interactions of the mesons are introduced in so-called nonlinear (NL) models or a density dependence (DD) of the the meson-nucleon couplings is utilized. These extensions of the original Walecka model [16] are essential to obtain reasonable properties of nuclei and nuclear matter. Applying certain approximations to the full many-body wave function of the system of interest, e.g., of Hartree, Hartree-Fock or Hartree-Fock-Bogoliubov type, a set of coupled equations is found which has to be solved self-consistently.

In the present work, new parameterisations of a relativistic EDF will be presented that include tensor couplings between nucleons and mesons in addition to the standard minimal couplings. Such an extension has been considered before in early applications of relativistic EDFs, see, e.g., Ref. [6], but it has been explored scarcely in depth. Including ρ -tensor, but no ω -tensor, contributions in relativistic Hartree-Fock calculations showed that the single-nucleon spectrum could be improved [17]. The interest in relativistic EDFs with tensor couplings has been grown recently as it can affect the description of surface properties of nuclei and (indirectly) the equation of state of nuclear matter. New parametrisations were developed in Ref. [18] for relativistic models with meson-nucleon couplings that depend on vector or scalar densities of the medium in various combinations, but using a more limited number of nuclear observables in the parameter fit as compared to the present work. The effects of tensor couplings on different properties of nuclei and, using the resulting equation of state (EOS) of dense matter, on neutron stars were explored in Ref. [19], however without a thorough determination of model parameters. Here, we shall embark on the development of a new relativistic EDF with minimal and tensor couplings using a careful selection of nuclear observables that are used in the fit of the model parameters. The medium dependence of the interaction is taken into account with a density dependence of the minimal couplings using the functional forms introduced in Ref. [11].

The content of this paper is structured as follows: The formalism of the relativistic energy density functional is presented in Section 2. The main quantities are introduced and the notation is established, in particular regarding the contribution with the tensor couplings. This section also provides the relevant equations for the description of spherical nuclei and nuclear matter in

two subsections. In Section 3 the approach to determine the model parameters is outlined. The functional form of the density dependent couplings is specified and the selection of the observables and nuclei in the fit is presented. Details of the fitting strategy are also given. Results and their discussion follow in Section 4, where properties of nuclei, nuclear matter, and neutron stars are considered in individual subsections. Finally, we close with a summary and outlook in Section 5.

2 Relativistic energy density functional

In a relativistic theory of nuclei and nuclear matter, nucleons and mesons are assumed to be the relevant degrees of freedom. Protons and neutrons are represented as Dirac spinors Ψ_η (with $\eta = \pi$ for protons and $\eta = \nu$ for neutrons) following Fermi statistics, whereas mesons are described by bosonic fields. The strong interaction between nucleons can be represented effectively by an exchange of mesons of different type. They often share their properties with those mesons of the same name and quantum numbers that are observed in experiments but are not necessarily identical. Actually, it is possible to describe the main features of the strong interaction by a rather small set of effective mesons that reduces the complexity of the calculations and the number of model parameters.

In relativistic EDFs, it is common practise to introduce an iso-scalar, Lorentz-scalar σ meson to model the attraction and an iso-scalar, Lorentz-vector ω meson to model the repulsion between nucleons. In order to take the isovector dependence of the interaction into account, an iso-vector, Lorentz-scalar δ meson and an iso-vector, Lorentz-vector ρ meson are also considered. The notation of these fields follows their properties, i.e., σ , ω^μ , $\vec{\delta}$, and $\vec{\rho}^\mu$ with Lorentz indices μ and the vector symbol for the three isovector components. The pion as another important meson is not included as it does not appear in the final equations after applying the basic approximations of the approach. Besides the above mentioned mesons, the photon field, denoted by the vector A^μ , completes the number of degrees of freedom to include also the electromagnetic interaction in the model.

The derivation of an EDF in a relativistic approach follows several steps that are detailed below. First, a Lagrangian density is formulated containing the contributions for the free propagation of the fields and their interaction. From it, the coupled field equations are derived that have to be solved self-consistently. This can be achieved in certain approximations and expressions for the energy of the system and other quantities of interest can be obtained. They are functions of the particle fields and their densities, so that the EDF is a generalized form of a density functional. It depends on a rather small number of parameters that need to be determined by appropriate procedures. In the formulas given below, we use a system of units where $\hbar = c = 1$. The value $\hbar = 197.3269804 \text{ MeV fm}/c$ is used for the conversion of units.

2.1 Lagrangian density, field equations, and energy density

The development of the relativistic EDF starts from a covariant Lagrangian density

$$\begin{aligned} \mathcal{L} = & \sum_{\eta=\pi,\nu} \bar{\Psi}_\eta (\gamma_\mu i\mathcal{D}^\mu - \sigma_{\mu\lambda} \mathcal{T}^{\mu\lambda} - \mathcal{M}_\eta) \Psi_\eta \\ & + \frac{1}{2} \left(\partial^\mu \sigma \partial_\mu \sigma - M_\sigma^2 \sigma^2 + \partial^\mu \vec{\delta} \cdot \partial_\mu \vec{\delta} - M_\delta^2 \vec{\delta} \cdot \vec{\delta} \right. \\ & \left. - \frac{1}{2} G^{\mu\lambda} G_{\mu\lambda} + M_\omega^2 \omega^\mu \omega_\mu - \frac{1}{2} \vec{H}^{\mu\lambda} \cdot \vec{H}_{\mu\lambda} + M_\rho^2 \vec{\rho}^\mu \cdot \vec{\rho}_\mu - \frac{1}{2} F^{\mu\lambda} F_{\mu\lambda} \right), \end{aligned} \quad (1)$$

with several contributions. Here, the field tensors of the mesons and of the massless electromagnetic field are given by the usual expressions;

$$G^{\mu\lambda} = \partial^\mu \omega^\lambda - \partial^\lambda \omega^\mu, \quad \vec{H}^{\mu\lambda} = \partial^\mu \vec{\rho}^\lambda - \partial^\lambda \vec{\rho}^\mu, \quad F^{\mu\lambda} = \partial^\mu A^\lambda - \partial^\lambda A^\mu. \quad (2)$$

The minimal coupling to the nucleons is realized by the corresponding terms in the covariant derivative

$$i\mathcal{D}^\mu = i\partial^\mu - \tilde{\Gamma}_\omega \omega^\mu - \tilde{\Gamma}_\rho \vec{\rho}^\mu \cdot \vec{\tau} - \Gamma_\gamma A^\mu \frac{1 + \tau_3}{2}, \quad (3)$$

for the Lorentz-vector mesons and the photon, and in the mass operator

$$\mathcal{M}_\eta = M_\eta - \tilde{\Gamma}_\sigma \sigma - \tilde{\Gamma}_\delta \vec{\delta} \cdot \vec{\tau}, \quad (4)$$

for the Lorentz-scalar mesons, respectively. The term in Eq. (1) with the quantity

$$\mathcal{T}^{\mu\lambda} = \frac{\Gamma_{T\omega}}{2M_\pi} G^{\mu\lambda} + \frac{\Gamma_{T\rho}}{2M_\pi} \vec{H}^{\mu\lambda} \cdot \vec{\tau}, \quad (5)$$

accounts for the additional tensor coupling of the nucleons to the mesons. Tensor couplings to the electromagnetic field are not included. The masses of the nucleons and the mesons are denoted by M_η ($\eta = \pi, \nu$) and M_j ($j = \sigma, \delta, \omega, \rho$), respectively. The isospin dependence is expressed with help of the isopin matrices τ_k ($k = 1, 2, 3$) in analogy to the Pauli spin matrices σ_k . The coupling factors $\tilde{\Gamma}_j$ in Eqs. (3), and (4) are assumed to be functionals of the nucleon fields Ψ_η , and $\bar{\Psi}_\eta = \Psi_\eta^\dagger \gamma^0$. In contrast, the tensor couplings $\Gamma_{T\omega}$, and $\Gamma_{T\rho}$, in Eq. (5) as well as the electromagnetic coupling Γ_γ in Eq. (3) are simple constants. The deviation by the proton mass in Eq. (5) is introduced to have dimensionless couplings $\Gamma_{T\omega}$ and $\Gamma_{T\rho}$.

The field equations of the nucleons, mesons, and the photon can be derived in the usual way from the Euler-Lagrange equations. However, they cannot be solved in the field-theoretical sense

and approximations are needed to arrive at tractable equations. The fields of the mesons and the photons are not quantized but considered as classical fields and will be denoted by the same symbols as in the original Lagrangian density (1) in the following. For the nucleons, the Hartree approximation is applied, i.e., the many-nucleon wave function Ψ of the system of interest is written as a product of single-nucleon states $\Psi_{\eta k_\eta m_\eta}$,

$$\Psi = \prod_{\eta=\pi,\nu} \prod_{k_\eta, m_\eta} w_{\eta k_\eta m_\eta} \Psi_{\eta k_\eta m_\eta}, \quad (6)$$

with occupation factors $w_{\eta k_\eta m_\eta}$. Only values of $w_{\eta k_\eta m_\eta} = 0$ and 1 are allowed. This condition reflects the fermionic nature of the nucleons. The meaning of the quantum numbers k_η , and m_η , is explained in Subsection 2.2. Only single-nucleon states of positive-energy are considered here, corresponding to the no-sea approximation and only a finite number of states contributes in the many-nucleon wave function.

For the dependence of the couplings $\tilde{\Gamma}_j$ in Eqs. (3), and (4), a so-called vector density dependence is assumed, i.e., with the approximation mentioned above, they become functions Γ_j of the vector density,

$$\varrho_v = \sqrt{j_\mu j^\mu}, \quad (7)$$

with the total current,

$$j^\mu = \sum_{\eta=\pi,\nu} \sum_{k_\eta, m_\eta} w_{i k_\eta m_\eta} \bar{\Psi}_{i k_\eta m_\eta} \gamma^\mu \Psi_{i k_\eta m_\eta}, \quad (8)$$

of the nucleons. The quantity ϱ_v is in fact a Lorentz scalar but has to be distinguished from the actual scalar density

$$\varrho_s = \sum_{\eta=\pi,\nu} \sum_{k_\eta, m_\eta} w_{i k_\eta m_\eta} \bar{\Psi}_{\eta k_\eta m_\eta} \Psi_{\eta k_\eta m_\eta}, \quad (9)$$

that is used for couplings with a scalar density dependence, c.f. Ref. [18].

In the actual application to nuclei and nuclear matter, a specific frame of reference is chosen and the covariance of the equations will be lost. In particular, a frame is chosen where the system is at rest, the couplings depend only on the zero-component of the current $\varrho_v = j^0$, and $\vec{j} = 0$. Since only static solutions without a change of isospin are considered, only the zero-component of the Lorentz-vector fields and a single component of the isovector quantities have to be taken into account, since all other components vanish. Assuming spherical symmetry, the field equation of the nucleons assumes the form of a modified Dirac equation,

$$\hat{H}_\eta \Psi_{\eta k_\eta m_\eta}(\vec{r}) = \left[\vec{\alpha} \cdot \hat{\vec{p}} + \beta (M_\eta - S_\eta) + V_\eta + i \vec{\gamma} \cdot \frac{\vec{r}}{r} T_\eta \right] \Psi_{\eta k_\eta m_\eta}(\vec{r}) = E_{\eta k_\eta} \Psi_{\eta k_\eta m_\eta}(\vec{r}), \quad (10)$$

with $\vec{\alpha} = \gamma^0 \vec{\gamma}$, and $\beta = \gamma^0$, for single-nucleon states of energy $E_{\eta k_\eta}$. The interaction with the meson and photon fields is expressed through the scalar potentials

$$S_\eta(\vec{r}) = \Gamma_\sigma \sigma + g_\eta \Gamma_\delta \delta, \quad (11)$$

vector potentials,

$$V_\eta(\vec{r}) = \Gamma_\omega \omega_0 + g_\eta \Gamma_\rho \rho_0 + \frac{1+g_\eta}{2} \Gamma_\gamma A_0 + V^{(R)}, \quad (12)$$

and tensor potentials,

$$T_\eta(\vec{r}) = -\frac{\Gamma_{T\omega}}{M_\pi} \frac{\vec{r}}{r} \cdot \vec{\nabla} \omega_0 - g_\eta \frac{\Gamma_{T\rho}}{M_\pi} \frac{\vec{r}}{r} \cdot \vec{\nabla} \rho_0, \quad (13)$$

with factors $g_\pi = 1$, and $g_\nu = -1$. The vector density dependence of the couplings generates the rearrangement contribution

$$V^{(R)}(\vec{r}) = \frac{d\Gamma_\omega}{dn^{(v)}} n_\omega \omega_0 + \frac{d\Gamma_\rho}{dn^{(v)}} n_\rho \rho_0 - \frac{d\Gamma_\sigma}{dn^{(v)}} n_\sigma \sigma - \frac{d\Gamma_\delta}{dn^{(v)}} n_\delta \delta, \quad (14)$$

in the vector potential (12). It contains derivatives of the couplings with respect to the vector density $n^{(v)} = \varrho_v$, as well as meson fields and source densities n_j ($j = \sigma, \delta, \omega, \rho$) that also appear in the meson field equations;

$$-\Delta \sigma + M_\sigma^2 \sigma = \Gamma_\sigma n_\sigma, \quad (15)$$

$$-\Delta \delta + M_\delta^2 \delta = \Gamma_\delta n_\delta, \quad (16)$$

$$-\Delta \omega_0 + M_\omega^2 \omega_0 = \Gamma_\omega n_\omega + \frac{\Gamma_{T\omega}}{m_p} \vec{\nabla} \cdot \vec{j}_\omega^{(t)}, \quad (17)$$

$$-\Delta \rho_0 + M_\rho^2 \rho_0 = \Gamma_\rho n_\rho + \frac{\Gamma_{T\rho}}{m_p} \vec{\nabla} \cdot \vec{j}_\rho^{(t)}, \quad (18)$$

for the non-vanishing components of the fields. They are given by

$$n_\sigma = n^{(s)} = n_\pi^{(s)} + n_\nu^{(s)}, \quad n_\delta = n_\pi^{(s)} - n_\nu^{(s)}, \quad (19)$$

$$n_\omega = n^{(v)} = n_\pi^{(v)} + n_\nu^{(v)} \};, \quad n_\rho = n_\pi^{(v)} - n_\nu^{(v)}, \quad (20)$$

with the vector and scalar densities;

$$n_\eta^{(v)}(\vec{r}) = \sum_{k_\eta, m_\eta} w_{\eta k_\eta m_\eta} n_{\eta k_\eta m_\eta}^{(v)} = \sum_{k_\eta, m_\eta} w_{\eta k_\eta m_\eta} \bar{\Psi}_{\eta k_\eta m_\eta} \gamma^0 \Psi_{\eta k_\eta m_\eta}, \quad (21)$$

and

$$n_\eta^{(s)}(\vec{r}) = \sum_{k_\eta, m_\eta} w_{\eta k_\eta m_\eta} n_{\eta k_\eta m_\eta}^{(s)} = \sum_{k_\eta, m_\eta} w_{\eta k_\eta m_\eta} \bar{\Psi}_{\eta k_\eta m_\eta} \Psi_{\eta k_\eta m_\eta}, \quad (22)$$

of nucleons, respectively. In Eqs. (17), and (18), also the divergences of the tensor currents

$$\vec{j}_\omega^{(t)} = \vec{j}_\pi^{(t)} - \vec{j}_\nu^{(t)}, \quad \vec{j}_\rho^{(t)} = \vec{j}_\pi^{(t)} - \vec{j}_\nu^{(t)}, \quad (23)$$

with,

$$\vec{j}_\eta^{(t)}(\vec{r}) = \sum_{k_\eta, m_\eta} w_{\eta k_\eta m_\eta} \vec{j}_{\eta k_\eta m_\eta}^{(t)} = \sum_{k_\eta, m_\eta} w_{\eta k_\eta m_\eta} \bar{\Psi}_{\eta k_\eta m_\eta} i \vec{\alpha} \Psi_{\eta k_\eta m_\eta}, \quad (24)$$

contribute to the source terms of the Lorentz-vector meson fields in Eqs. (17), and (18). Note that these tensor currents are not the vector part of the usual four-currents,

$$j_\eta^\mu(\vec{r}) = \sum_{k_\eta, m_\eta} w_{\eta k_\eta m_\eta} \bar{\Psi}_{\eta k_\eta m_\eta} \gamma^\mu \Psi_{\eta k_\eta m_\eta}. \quad (25)$$

Finally, the field equation for the electromagnetic field is given by the usual Poisson's equation

$$-\Delta A_0 = \Gamma_\gamma n_\gamma, \quad (26)$$

with the source density $n_\gamma = n_\pi^{(v)}$.

In the application to nuclear matter, there is no spatial dependence of the source densities and meson fields. They become constants and there are no contributions from the tensor currents in Eqs. (17), and (18). The field equations are solved trivially and the tensor potential (13) in the Dirac equation (10) vanishes too. Nucleon states are then described by plane waves.

The energy density of the system can be obtained as a component of the energy-momentum tensor

$$T^{\mu\lambda} = \sum_\varphi \frac{\partial \mathcal{L}}{\partial(\partial_\mu \varphi)} \partial^\lambda \varphi - g^{\mu\lambda} \mathcal{L}, \quad (27)$$

where the sum runs over all fields $\varphi = \Psi_{\eta k_\eta m_\eta}, \bar{\Psi}_{\eta k_\eta m_\eta}, \sigma, \delta, \omega_0, \rho_0, A_0$, and the metric tensor is $g^{\mu\lambda} = \text{diag}(-1, 1, 1, 1)$. It can be expressed as a sum,

$$\varepsilon(\vec{r}) = T^{00} = \varepsilon_{\text{nucleon}}(\vec{r}) + \varepsilon_{\text{field}}(\vec{r}), \quad (28)$$

with the contribution

$$\varepsilon_{\text{nucleon}}(\vec{r}) = \sum_{\eta=\pi, \nu} \sum_{k_\eta, m_\eta} w_{\eta k_\eta m_\eta} E_{\eta k_\eta} n_{\eta k_\eta m_\eta}^{(v)}, \quad (29)$$

of the nucleons and that of the fields

$$\begin{aligned} \varepsilon_{\text{field}}(\vec{r}) = & \frac{1}{2} \left(\vec{\nabla}\sigma \cdot \vec{\nabla}\sigma + M_\sigma^2 \sigma^2 + \vec{\nabla}\delta \cdot \vec{\nabla}\delta + M_\delta^2 \delta^2 \right. \\ & \left. - \vec{\nabla}\omega_0 \cdot \vec{\nabla}\omega_0 - M_\omega^2 \omega_0^2 - \vec{\nabla}\rho_0 \cdot \vec{\nabla}\rho_0 - M_\rho^2 \rho_0^2 - \vec{\nabla}A_0 \cdot \vec{\nabla}A_0 \right) - V^{(R)} n^{(v)} \end{aligned} \quad (30)$$

with an explicit rearrangement term.

2.2 Spherical nuclei

For describing nuclei, the coupled differential equations (10) for the single-nucleon wave functions, and (15) - (26), have to be solved self-consistently. In the case of spherical symmetry, it is convenient to represent the single-nucleon wave functions as

$$\Psi_{\eta k_\eta m_\eta}(\vec{r}) = \frac{1}{r} \begin{pmatrix} F_{\eta k_\eta}(r) \mathcal{Y}_{\kappa_\eta m_\eta}(\hat{r}) \\ i G_{\eta k_\eta}(r) \mathcal{Y}_{-\kappa_\eta m_\eta}(\hat{r}) \end{pmatrix}, \quad (31)$$

with radial functions $F_{\eta k_\eta}$, and $G_{\eta k_\eta}$, and tensor spherical harmonics,

$$\mathcal{Y}_{\kappa m}(\hat{r}) = \sum_{m_l m_s} (l_\kappa m_l s m_s | j_\kappa m) Y_{l_\kappa m_l}(\hat{r}) \chi_{s m_s}, \quad (32)$$

in the upper and lower components of the Dirac spinor. Each state is identified by the index $\eta = \pi, \nu$, and two quantum numbers n_η , and κ_η , that are collectively denoted as k_η , and a total angular momentum projection m_η . The first, $n_\eta = 0, 1, 2, \dots$, is the principal quantum number related to the number of nodes of the function $F_{\eta k_\eta}$; the second, $\kappa_\eta = \pm 1, \pm 2, \dots$, defines the total angular momentum $j_\kappa = |\kappa| - 1/2$ and the orbital angular momentum $l_\kappa = j_\kappa - \kappa / (2|\kappa|)$ of a state. Then the Dirac equation (10) is equivalent to the set of two coupled differential equations;

$$(E_{\eta k_\eta} - V_\eta - M_\eta + S_\eta) F_{\eta k_\eta} + \left(\frac{d}{dr} + \frac{\kappa_k}{r} - T_\eta \right) G_{\eta k_\eta} = 0, \quad (33)$$

and,

$$\left(\frac{d}{dr} - \frac{\kappa_k}{r} + T_\eta \right) F_{\eta k_\eta} - (E_{\eta k_\eta} - V_\eta + M_\eta - S_\eta) G_{\eta k_\eta} = 0, \quad (34)$$

for the radial functions that have to be solved with the boundary conditions $F_{\eta k_\eta}(0) = G_{\eta k_\eta}(0) = 0$, and $\lim_{r \rightarrow 0} F_{\eta k_\eta}(r) = \lim_{r \rightarrow 0} G_{\eta k_\eta}(r) = 0$.

The representation (31) of the single-nucleon wavefunctions leads to the expressions

$$n_{\eta k_{\eta} m_{\eta}}^{(s)}(r) = \frac{1}{4\pi r^2} \left[|F_{\eta k_{\eta}}(r)|^2 - |G_{\eta k_{\eta}}(r)|^2 \right] \quad (35)$$

and

$$n_{\eta k_{\eta} m_{\eta}}^{(v)}(r) = \frac{1}{4\pi r^2} \left[|F_{\eta k_{\eta}}(r)|^2 + |G_{\eta k_{\eta}}(r)|^2 \right] \quad (36)$$

for the scalar and vector single-nucleon densities in Eqs. (22), and (21), respectively, if an average over the quantum number m_{η} is applied. This procedure is used to obtain spherical source densities in the field equations for the mesons and the photon in case that sub-shells of given j are not completely filled. The vector densities are normalized as,

$$\int d^3r n_{\eta k_{\eta} m_{\eta}}^{(v)}(r) = 1, \quad (37)$$

but, there is no such condition for the scalar densities. The single-nucleon tensor currents have only a component in radial direction in a spherical system. Then one can define

$$n_{\eta k_{\eta} m_{\eta}}^{(t)} = \frac{1}{4\pi r^2} \left[F_{\eta k_{\eta}}^*(r) G_{\eta k_{\eta}}(r) + F_{\eta k_{\eta}}(r) G_{\eta k_{\eta}}^*(r) \right], \quad (38)$$

so that,

$$\vec{j}_{\eta k_{\eta} m_{\eta}}^{(t)} = n_{\eta k_{\eta} m_{\eta}}^{(t)} \frac{\vec{r}}{r}, \quad \text{and} \quad \vec{\nabla} \cdot \vec{j}_{\eta k_{\eta} m_{\eta}}^{(t)} = \frac{1}{r^2} \frac{d}{dr} \left(r^2 n_{\eta k_{\eta} m_{\eta}}^{(t)} \right), \quad (39)$$

in Eq. (24) after applying the averaging procedure. The occupation factors in the calculation of the densities are determined such that,

$$\sum_{k_{\pi}, m_{\pi}} w_{\pi k_{\pi} m_{\pi}} = Z, \quad \text{and} \quad \sum_{k_{\nu}, m_{\nu}} w_{\nu k_{\nu} m_{\nu}} = N, \quad (40)$$

with the proton and neutron numbers Z and N of the nucleus, respectively, with mass number $A = Z + N$.

The energy of the nucleus is finally obtained as

$$E_{\text{nucleus}} = E_{\text{sp}} + E_{\text{field}} - E_{\text{corr}}, \quad (41)$$

with the contributions of the single-particle states

$$E_{\text{sp}} = \sum_{\eta=\pi,\nu} \sum_{k_\eta, m_\eta} w_{\eta k_\eta m_\eta} E_{\eta k_\eta}, \quad (42)$$

and of the fields,

$$E_{\text{field}} = \frac{1}{2} \int d^3r \left\{ \Gamma_\sigma n_\sigma \sigma + \Gamma_\delta n_\delta \delta - \Gamma_\gamma n_\gamma A_0 \right. \\ \left. - \left[\Gamma_\omega n_\omega + \frac{\Gamma_{T\omega}}{M_p} \vec{\nabla} \cdot \vec{j}_{T\omega} \right] \omega_0 - \left[\Gamma_\rho n_\rho + \frac{\Gamma_{T\rho}}{M_p} \vec{\nabla} \cdot \vec{j}_{T\rho} \right] \rho_0 - V^{(R)} n^{(v)} \right\}, \quad (43)$$

where the field equations were exploited after a partial integration using Eq. (30). Since the translational symmetry is broken, a correction for the center-of-mass motion has to be applied. It is calculated as the expectation value

$$E_{\text{corr}} = \langle \Psi | \frac{\vec{P}^2}{2M(Z, N)} | \Psi \rangle, \quad (44)$$

of the total momentum

$$\vec{P} = \sum_{j=1, Z} \vec{p}_{\pi j} + \sum_{j=1, N} \vec{p}_{\nu j}, \quad (45)$$

in non-relativistic form with the total mass $M(Z, N) = ZM_\pi + NM_\nu$ of the nucleus, neglecting the binding energy.

For the numerical solution of the coupled differential equations (33), and (34), the Lagrange-mesh technique is utilized, see Ref. [20] and references therein. This approach combines the virtues of an expansion in terms of basis functions and a discretization on a grid. At the same time it is numerically efficient and precise. The radial wave functions are represented with their values at grid points $r_i = hx_i^{(\alpha)}$, where h is a scale parameter, and $x_i^{(\alpha)}$ are the zeroes $i = 1, \dots, N_{\text{zero}}$ of the Laguerre polynomials $L_N^{(\alpha)}(x)$ with $N_{\text{zero}} = 25$, and $\alpha = 2|\kappa|$. The scale parameter h is chosen such that the largest zero of $L_N^{(0)}$ is at a radius $r = 0.95R$, with $R = r_0 A^{1/3} + 10$ fm, and $r_0 = 1.2$ fm depending on the mass number A of the nucleus. The field equations of the mesons, (15) - (18), and the photon, (26), are solved by expanding the fields and sources in terms of Riccati-Bessel functions. Special care has to be taken for the electromagnetic potential A_0 to obtain the correct asymptotic behavior for large radii. For more details on the numerical techniques, see Ref. [20].

2.3 Nuclear matter

The solution of the field equations (10), (15) - (18), and (26) simplifies considerably in homogeneous and isotropic nuclear matter. The source densities and meson fields become constants. The electromagnetic field has to be discarded and all contributions of the tensor terms vanish. Nucleons are described by plane waves of momentum k_η following the dispersion relation

$$E_{\eta k_\eta} = \sqrt{k_\eta^2 + (M_\eta^*)^2} + V_\eta, \quad (46)$$

where the Dirac effective mass

$$M_\eta^* = M_\eta - S_\eta, \quad (47)$$

and constant scalar and vector potentials (11), and (12), appear. At zero temperature, all relevant quantities can be calculated analytically. The scalar and vector densities assume the form;

$$n_\eta^{(s)} = \gamma_\eta \int_0^{k_\eta^*} \frac{d^3 k_\eta}{(2\pi)^3} \frac{M_\eta^*}{\sqrt{(k_\eta)^2 + (M_\eta^*)^2}} = \frac{\gamma_\eta M_\eta^*}{4\pi^2} \left[k_\eta^* \mu_\eta^* - (M_\eta^*)^2 \ln \frac{k_\eta^* + \mu_\eta^*}{M_\eta^*} \right], \quad (48)$$

and,

$$n_\eta^{(v)} = \gamma_\eta \int_0^{k_\eta^*} \frac{d^3 k_\eta}{(2\pi)^3} = \frac{g_\eta}{6\pi^2} (k_\eta^*)^3, \quad (49)$$

in the continuum approximation, with the spin degeneracy factor $\gamma_\eta = 2$. The Fermi momenta k_η^* are related to the effective chemical potentials

$$\mu_\eta^* = \mu_\eta - V_\eta = \sqrt{(k_\eta^*)^2 + (M_\eta^*)^2}, \quad (50)$$

of the nucleons.

The energy density of cold nuclear matter can be written as,

$$\varepsilon = \sum_{\eta=\pi,\nu} \frac{1}{4} \left[3\mu_\eta^* n_\eta^{(v)} + M_\eta^* n_\eta^{(s)} \right] + \frac{1}{2} \sum_{j=\sigma,\delta,\omega,\rho} C_j n_j^2, \quad (51)$$

with the coupling-to-mass ratios

$$C_j = \frac{\Gamma_j^2}{M_j^2}. \quad (52)$$

The pressure

$$P = \sum_{\eta=\pi,\nu} \frac{1}{4} \left[\mu_\eta^* n_\eta^{(v)} - M_\eta^* n_\eta^{(s)} \right] - \frac{1}{2} \sum_{j=\sigma,\delta} (C_j + n^{(v)} C_j') n_j^2 + \frac{1}{2} \sum_{j=\omega,\rho} (C_j + n^{(v)} C_j') n_j^2, \quad (53)$$

also depends on the derivatives

$$C'_j = \frac{dC_j}{dn^{(v)}}, \quad (54)$$

and can be derived using the thermodynamic definition $P = d(\varepsilon/n^{(v)})/dn^{(v)}$, or from the energy-momentum tensor (27), as $P = (1/3) \sum_{\mu=1}^3 T^{\mu\mu}$. It is easily shown that energy density and pressure fulfill the Hugenberg-van-Hove relation [21]

$$\varepsilon + P = \sum_{\eta=\pi,\nu} \mu_\eta n_\eta^{(v)}, \quad (55)$$

since the rearrangement terms in the pressure combine with those in the chemical potentials μ_η appearing in Eq. (50).

The energy density (51), and pressure (53), are functions of two independent densities, the proton and neutron vector densities $n_\pi^{(v)}$, and $n_\nu^{(v)}$. Alternatively, they can be regarded as functions of the baryon density

$$n_b = \varrho_v = n^{(v)} = n_\nu^{(v)} + n_\pi^{(v)}, \quad (56)$$

and the neutron-proton asymmetry

$$\alpha = \frac{n_\nu^{(v)} - n_\pi^{(v)}}{n_b}, \quad (57)$$

that lies inside the interval $[-1, +1]$. Then it is convenient to define the energy per nucleon

$$\frac{E}{A}(n_b, \alpha) = \frac{\varepsilon}{n_b} - M_{\text{nuc}}, \quad (58)$$

subtracting the average nucleon mass $M_{\text{nuc}} = (M_\nu + M_\pi)/2$. A second derivative,

$$E_{\text{sym}}(n_b) = \frac{1}{2} \left. \frac{d^2}{d\alpha^2} \frac{E}{A} \right|_{\alpha=0}, \quad (59)$$

gives the symmetry energy. It characterizes how the isospin dependence of the energy per nucleon changes with the baryon density.

3 Determination of model parameters

The relativistic EDF depends on several parameters: the masses of the particles and the coefficients that describe the strength of the couplings and their density dependence. The masses of the nucleons and the mesons, except that of the σ meson are usually chosen to be identical or close to the experimental values. In the present application of the relativistic EDF the δ meson is not included in the model. The remaining fixed mass parameters of the nucleons and Lorentz-vector mesons are

Table 1 Masses of nucleons and Lorentz-vector mesons used in the model parameterisations of this work.

particle	p	n	ω	ρ
mass in MeV	938.27208816	939.5654205	783	763

given in Table 1 for the models in this work. The mass of the σ meson is used as an independent parameter because it is not well defined by experimental data and affects the surface properties of nuclei.

The actual values of the model parameters are determined by fitting selected observables of finite nuclei that are sensitive to different contributions in the EDF and are obtained more-or-less directly from experiment. More indirectly obtained quantities, e.g., characteristic nuclear matter parameters, that can depend strongly on the extraction method from actual experimental data, or other constraints, e.g., from ab-initio calculations of nuclear matter or from astrophysical observations, are not used in this procedure. A comparison to these data will be performed after the model parameters have been determined.

3.1 Functional form of density dependent couplings

The meson-nucleon couplings Γ_j are assumed to be functions of the vector density $\varrho_v = n^{(v)}$. In this work, the functional form of the dependence is chosen as introduced originally in [11] with

$$\Gamma_j(\varrho) = \Gamma_j^{(0)} f_j(x), \quad (60)$$

where $\Gamma_j^{(0)} = \Gamma_j(\varrho_{\text{ref}})$ is the coupling at a reference density ϱ_{ref} and the functions f_j depend on the parameter $x = \varrho_v/\varrho_{\text{ref}} \geq 0$. For the isoscalar mesons $j = \sigma, \omega$ a rational form

$$f_j(x) = a_j \frac{1 + b_j(x + d_j)^2}{1 + c_j(x + d_j)^2}, \quad (61)$$

with four coefficients a_j , b_j , c_j , and d_j is used. To avoid a pole in f_j , the coefficients c_j , and d_j have to be non-negative. The constraints $f_j(1) = 1$, and $f_j''(0) = 0$, reduce the number of independent coefficients to two with $a_j = [1 + c_j(1 + d_j)^2]/[1 + b_j(1 + d_j)^2]$, and $c_j = 1/(3d_j^2)$. The coupling function for the isovector mesons $j = \rho$ is chosen as an exponential,

$$f_\rho(x) = \exp[-a_\rho(x - 1)], \quad (62)$$

with only one coefficient a_ρ . Obviously, other functions can be and have been used to describe the density dependence of the couplings, see, e.g., Ref. [15]. Also a dependence on the scalar density $n^{(s)}$ or other densities can be explored, see, e.g., Ref. [18].

In the model parameterisations of this work, there are three independent parameters for the isoscalar mesons σ and for ω and two for the isovector meson ρ , thus eight parameters in total that need to be determined for the nuclear-matter calculations besides the mass of the σ meson. In the actual fitting procedure, the saturation density of symmetric nuclear matter n_{sat} is used as reference density ϱ_{ref} , but the couplings $\Gamma_j^{(0)}$ at ϱ_{ref} and the coefficients a_j , b_j , c_j , and d_j are not used directly as independent quantities that are varied. Instead, the following characteristic nuclear matter parameters are selected as variable quantities:

1. the effective Dirac mass at saturation M_{sat}^* ,
2. the binding energy per nucleon at saturation B_{sat} ,
3. the incompressibility coefficient at saturation K ,
4. the symmetry energy at saturation J ,
5. the slope parameter of the symmetry energy at saturation L .

Together with the condition of vanishing pressure at n_{sat} , this gives already six parameters. The remaining two quantities that are used in the actual fit are the ratios

$$r_{10} = \frac{f'_\omega(1)}{f_\omega(1)}, \quad \text{and} \quad r_{21} = \frac{f''_\omega(1)}{f'_\omega(1)}, \quad (63)$$

with the density dependent function $f_\omega(x)$ of the ω meson. It is assumed that the coupling functions are decreasing with the density, hence $f'_\omega(1)$ has to be smaller than zero. Then the functional form of f_ω leads to the constraint $-3 < r_{21} < 0$ for the second ratio in Eq. (63). The actual procedure of the parameter conversion is given in detail in Appendix A.

In the description of finite nuclei, two additional tensor couplings $\Gamma_{T\omega}$ and $\Gamma_{T\rho}$ appear if the tensor terms in the Lagrangian density (1) are considered. These constants are used directly as independent parameters in the fit. Hence there are in total 11 (9) independent parameters in models with (without) tensor couplings taking into account the mass of the σ meson M_σ as another undetermined quantity.

3.2 Observables and nuclei in the fit

The choice of the observables that are included in fitting the model parameters will affect the final results. Only quantities should be selected that are well determined by experiments. Different

strategies are followed by various authors. In the present work, the following nuclear observables of a nucleus are used:

1. the binding energy B ,
2. the charge radius r_c ,
3. the diffraction radius r_d ,
4. the surface thickness σ ,
5. the root-mean-square radius r_n of a single valence neutron level above a shell closure,
6. the spin-orbit splitting ΔE_{so} for two levels of a nucleon η in states with the same quantum numbers n_η and l_η but different $j_\eta = l_\eta \pm 1/2$,
7. the constraint isoscalar monopole giant resonance energy E_{mono} .

They are calculated after the coupled equations for a nucleus (Z, N) are solved and can be compared with experimental data.

3.2.1 Values of observables from theory

The binding energy is derived as

$$B(Z, N) = M(Z, N) - E_{\text{nucleus}}(Z, N) , \quad (64)$$

from the energy (41). The charge radius, the diffraction radius, and the surface thickness are obtained from the charge form factor of a spherical nucleus. It depends on a momentum \vec{q} and is calculated as,

$$F_{Z,N}(q) = [F_Z(q)F_\pi(q) + F_N(q)F_\nu(q)] F_{\text{corr}}(q) , \quad (65)$$

with form factors of the proton and neutron distributions in the nucleus, single-nucleon form factors and a center-of-mass correction. The density distributions (36) of neutron and protons are used to calculate the form factors

$$F_Z(q) = \int d^3r \sum_{k_\pi, m_\pi} w_{\pi k_\pi m_\pi} n_{\pi k_\pi m_\pi}(\vec{r}) \exp(i\vec{q} \cdot \vec{r}) , \quad (66)$$

and,

$$F_N(q) = \int d^3r \sum_{k_\nu, m_\nu} w_{\nu k_\nu m_\nu} n_{\nu k_\nu m_\nu}(\vec{r}) \exp(i\vec{q} \cdot \vec{r}) , \quad (67)$$

Table 2 Coefficients [5, 22] in the parameterisation (68) of the nucleon form factors $F_\eta(q)$ ($\eta = \pi, \nu$).

k	$A_{\pi k}$	$B_{\pi k}$ [fm ²]	$A_{\nu k}$	$B_{\nu k}$ [fm ²]
1	0.312	0.16667	1	0.04833
2	1.312	0.06658	-1	0.05833
3	-0.709	0.02269	0	0
4	0.085	0.006485	0	0

that are spherically symmetric in momentum space due to the spherical symmetry of the density distributions. The single-nucleon form factors are parameterized [5, 22] as

$$F_\eta(q) = \sum_{k=1}^4 \frac{A_{\eta k}}{1 + B_{\eta k} q^2}, \quad (68)$$

with coefficients $A_{\eta k}$, and $B_{\eta k}$, that are given in Table 2. The center-of-mass correction

$$F_{\text{corr}}(q) = \exp \left[\frac{3q^2}{16E_{\text{corr}}M(Z, N)} \right], \quad (69)$$

depends on the center-of-mass correction (44) of the energy. The charge density of the nucleus is finally obtained from

$$n_{\text{charge}}(r) = \int \frac{d^3q}{(2\pi)^3} F_{Z, N}(q) \exp(-i\vec{q} \cdot \vec{r}). \quad (70)$$

It is used to calculate the root-mean-square charge radius

$$r_c = \left[\frac{1}{Z} \int d^3r r^2 n_{\text{charge}}(r) \right]^{1/2}, \quad (71)$$

of the nucleus. The form factor (65) at zero momentum has the values $F_{Z, N}(0) = Z$ and decreases with q until it reaches a first zero at q_0 . This value is used to obtain the diffraction radius

$$r_d = \frac{4.493409458}{q_0}, \quad (72)$$

where the numerical factor is the first zero of the Bessel function $j_1(x) = -j'_0(x)$. Further increasing q leads to the first minimum of $F_{Z, N}(q)$ at q_m that is used to calculate the surface thickness

$$\sigma(Z, N) = \frac{1}{q_m} \left\{ 2 \ln \left[\frac{ZF_{\text{box}}(q_m)}{F_{Z, N}(q_m)} \right] \right\}^{1/2}, \quad (73)$$

with the form factor $F_{\text{box}}(q) = 3j_1(qr_d)/(qr_d)$ of a box of radius r_d , c.f. Ref. [5], and Eq. (18a) of Ref. [6] with corrections. The root-mean-square radius of a single-neutron state is defined as

$$r_\nu = \left[\int d^3r r^2 n_{\nu k_\nu m_\nu}(r) \right]^{1/2}, \quad (74)$$

similar as the charge radius (71). The spin-orbit splitting is given by the difference

$$\Delta E_{so}(\eta n_\eta l_\eta) = E_{\eta k_\eta^-} - E_{\eta k_\eta^+}, \quad (75)$$

of the single-nucleon energies of the levels with identical principal quantum number n_η , and $k_\eta^\pm = (n_\eta, \kappa_\eta^\pm)$, where $\kappa_\eta^\pm = (j_\eta^\pm - l_\eta)(2j_\eta^\pm + 1)$ for $j_\eta^\pm = l_\eta \pm 1/2$. The constraint isoscalar monopole giant resonance energy E_{mono} is obtained from a constraint calculation of the nucleus as described in Ref. [1]. A contribution

$$V_\lambda = -\lambda r^2, \quad (76)$$

with parameter λ , is added to the vector potential (12) of the nucleons and the coupled equations for the fields are solved self-consistently for given λ . Then the root-mean-square radius

$$\langle r^2 \rangle_\lambda = \int d^3r r^2 n_\lambda^{(v)}(\vec{r}), \quad (77)$$

of the total vector density $n_\lambda^{(v)}$ of the obtained configuration is calculated. The constraint isoscalar monopole giant resonance energy

$$E_{\text{mono}} = \sqrt{\frac{m_1}{m_{-1}}}, \quad (78)$$

can be found from the ratio of moments

$$m_1 = 2 \frac{\hbar^2}{m_{\text{nuc}}} \langle r^2 \rangle_{\lambda=0}, \quad (79)$$

and,

$$m_{-1} = \frac{1}{2} \frac{d}{d\lambda} \langle r^2 \rangle_\lambda \Big|_{\lambda=0}. \quad (80)$$

In the actual calculation, a five-point formula is used with $\lambda_n = n \times 0.125$ keV and $n = -2, -1, 0, 1, 2$ to calculate the derivative.

3.2.2 Selection of nuclei and experimental data

The description of nuclei with the relativistic EDF presented here can only be applied to nuclei with spherical symmetry. Also pairing effects are not taken into account. Thus a comparison of theory and experiment can be reasonably performed only for magic or semi-magic nuclei. This limits the amount of data that can be included in the fit of the model parameters. However,

this restriction is not too severe since the essential features of strongly interacting systems are sufficiently well constrained by the selection of the fitted data in this approach. In order to fix the isospin dependence of the effective interaction well, nuclei with large $|N - Z|$ should be included, preferably on both sides of the valley of stability. The nuclei actually considered can be read off from Tables 6, and 7. There are 18 (semi)magic nuclei and 2 with one valence neutron above a doubly magic core. Not all data from the list in Subsection 3.2 are always available for all nuclei.

Binding energies $B(Z, N)$ of nuclei are obtained from the Atomic Mass Evaluation 2020 [23] by multiplying the binding energy per nucleon given there with the mass number $A = Z + N$. These data are tabulated in Table 6. Experimental data for the charge radius, diffraction radius, surface thicknesses and neutron radii can be found in Table 7. The charge radii and quantities related to the charge form factor are extracted from [24–27] using the Fourier-Bessel parameterisation if available. The experimental valence neutron radii are taken from [28, 29]. Experimental spin-orbit splittings are given in Table 8. They are derived from the nuclear level schemes collected at the National Nuclear Data Center [30, 31]. Experimental constraint isoscalar monopole giant resonance energies [32] are listed in Table 9 for selected nuclei. The choice of the constraint isoscalar monopole giant resonance energy as an observable in the fit greatly helps to obtain a reasonable incompressibility coefficient K of nuclear matter, a quantity that is often set to a predefined value since it is not well constrained by other quantities of nuclei.

3.3 Objective function and uncertainties

In order to determine optimal parameter values of the relativistic EDF, an appropriate fitting procedure has to be applied. This is usually done by minimizing an objective function that quantifies the deviation of the theoretical predictions for certain observables from experimental data. A crucial question is the size of the uncertainties that are used for the different observables, e.g., in a χ^2 minimization. In the parameter fit of an EDF it is generally not reasonable to use the experimental uncertainties because they are for most quantities much smaller than the precision that can be achieved by an EDF. Instead, often some 'reasonable' values are chosen that may, however, not reflect the 'true' uncertainties that are expected for such an EDF. Thus, in the present work a fitting scheme is employed that also attempts to determine the uncertainties, c.f. Ref. [18].

In the present approach to fit the model parameters, $N_{\text{obs}} = 7$ types of observables are considered as specified in Section 3.2 with $N_i^{(\text{obs})}$ data per observable ($i = 1, \dots, N_{\text{obs}}$). Thus an objective function,

$$\chi^2(\{p_k\}) = \sum_{i=1}^{N_{\text{obs}}} \chi_i^2(\{p_k\}), \quad (81)$$

is defined that depends on N_{par} parameters p_k ($k = 1, \dots, N_{\text{par}}$) with $N_{\text{par}} = 11$ (9) for models with (without) tensor couplings. The contributions for each observable \mathcal{O}_i to (81) are given by the standard expression

$$\chi_i^2(\{p_k\}) = \sum_{n=1}^{N_i^{(\text{obs})}} \left[\frac{\mathcal{O}_i^{(\text{model})}(n, \{p_k\}) - \mathcal{O}_i^{(\text{exp})}(n)}{\Delta\mathcal{O}_i} \right]^2, \quad (82)$$

where the $n = 1, \dots, N_i^{(\text{obs})}$ data of an observable \mathcal{O}_i depend on the parameters $\{p_k\}$. The total number of data is given by

$$N_{\text{data}} = \sum_{i=1}^{N_{\text{obs}}} N_i^{(\text{obs})}, \quad (83)$$

and thus the number of degrees of freedom is $N_{\text{dof}} = N_{\text{data}} - N_{\text{par}}$.

The uncertainties for each observable \mathcal{O}_i are denoted by $\Delta\mathcal{O}_i$. Since binding energies of stable nuclei are much more precisely known than those of exotic nuclei, their uncertainties vary over a large range. Thus the uncertainty of the observable $\mathcal{O}_i = B(Z, N)$ in the function (82) is assumed to compose of two contributions as,

$$\Delta\mathcal{O}_i = \left[\left(\Delta\mathcal{O}_i^{(\text{exp})} \right)^2 + \left(\Delta\mathcal{O}_i^{(\text{fit})} \right)^2 \right]^{1/2}, \quad (84)$$

with an experimental uncertainty $\Delta\mathcal{O}_i^{(\text{exp})}$ and a fit uncertainty $\Delta\mathcal{O}_i^{(\text{fit})}$. For all other observables, the experimental uncertainty is neglected in the fits of this work. A reasonable estimate of the fit uncertainties will be obtained if,

$$\chi^2(\{p_k\})/N_{\text{dof}} = 1, \quad (85)$$

and,

$$\frac{\chi_i^2(\{p_k\})}{N_i^{(\text{obs})}} = \frac{\chi^2(\{p_k\})}{N_{\text{data}}}, \quad (86)$$

i.e., each observable contributes on the average equally to the total χ^2 . These conditions allow to determine the fit errors $\Delta\mathcal{O}_i^{(\text{fit})}$ during the fit by a rescaling. Thus the general fit procedure proceeds in two steps: variation of the model parameter to minimize (81) until a certain convergence is reached, and a rescaling of the fit uncertainties. These two steps are executed repeatedly until the fit uncertainties and model parameters have converged to the desired precision. To find the optimal values of the model parameters in their space of dimension N_{par} , a simplex method [33] was employed as in Ref. [18]. It only relies on values of the χ^2 function and does not need derivatives. Once the minimum of the total χ^2 function is found, the solution can be represented as a vector $\vec{p}^{\text{min}} = (p_1^{\text{min}}, \dots, p_{N_{\text{par}}}^{\text{min}})$ in the space of parameters. A true (local) minimum of χ^2 is reached when

the matrix of second derivatives,

$$\mathcal{M}_{ij} = \frac{1}{2} \left. \frac{\partial^2 \chi^2}{\partial p_i \partial p_j} \right|_{\vec{p}_{\min}}, \quad (87)$$

has only positive eigenvalues. If this is not the case, the eigenvectors with negative eigenvalues indicate directions for a further reduction of χ^2 . This information is used every now and then to accelerate the minimization. However, the calculation of \mathcal{M}_{ij} is expensive as it needs $2N_{\text{par}}^2 + 1$ function evaluations. Finally, it is possible to determine the uncertainty

$$\Delta \mathcal{O} = \sqrt{(\Delta \mathcal{O})^2}, \quad (88)$$

of any observable \mathcal{O} and the correlation coefficient

$$c_{\mathcal{O}_1 \mathcal{O}_2} = \frac{\overline{\Delta \mathcal{O}_1 \Delta \mathcal{O}_2}}{\sqrt{(\Delta \mathcal{O}_1)^2 (\Delta \mathcal{O}_2)^2}}, \quad (89)$$

between two observables \mathcal{O}_1 and \mathcal{O}_2 from

$$\overline{\Delta \mathcal{O}_1 \Delta \mathcal{O}_2} = \sum_{ij} \frac{\partial \mathcal{O}_1}{\partial p_i} (\mathcal{M}^{-1})_{ij} \frac{\partial \mathcal{O}_2}{\partial p_j}, \quad (90)$$

that contains the inverse of the matrix \mathcal{M} and first derivatives of the observables with respect to the parameters.

3.4 Types of energy density functionals

The main aim of the present work is the development of a new parameterisation of a relativistic EDF with tensor couplings, denoted by 'DDT' in the following, in addition to the usual minimal couplings of the mesons to the nucleons. In order to compare the main differences of this EDF to a model without tensor interactions, the results of the DD2 model [34] will be shown, that uses the same form of the relativistic EDF.

A particular issue is the effect of exchange contributions that are neglected in the relativistic EDF, which is constructed in Hartree approximation from the Lagrangian density. This concerns particularly the Coulomb interaction. The source density of the electromagnetic field, that is found by solving Eq. (26), includes the charge distribution of all protons so that the Coulomb field in the vector potential (12), which a proton feels in the mean-field created by all particles, also contains a self-interaction contribution that would not arise with the proper use of an antisymmetrized many-body wave function. The exchange term is sometimes added in form of the Slater approximation

[35]. However, this is not done in this work. As an alternative, a simple correction to reduce the self-interaction term is to multiply the field A_0 in Eq. (12) by the factor $(Z-1)/Z$ in the calculation of nuclei, as used in the DD2 parameterisation. Then the vector potential $V_\pi(\vec{r})$ has the correct asymptotic form for large radii when a proton is separated from a nucleus. To study the effect of this modification, a variation with this reduction factor, DDTC, of the original DDT parameterisation is also developed.

A more detailed consideration of the contributions to the energy of a nucleus reveals, however, that it is admissible to neglect the exchange part in the Coulomb energy. In fact, there are two contributions that in total compensate for the exchange term. On the one hand, there is the Coulomb displacement energy of analog states in mirror nuclei that, in the mean-field approximation, e.g., for the ^{41}Sc - ^{41}Ca pair is smaller by about 7%. This is known as the Nolen-Schiffer anomaly [36] which is solved by the taking into account the charge symmetry breaking (CSB) contribution in the nucleon-nucleon interaction, and long-range correlation (LRC) effects [37]. Ignoring the factor $(Z-1)/Z$ in the Coulomb direct term, which leads to including the Coulomb self-interaction terms, and ignoring the Coulomb exchange term corresponds to including the contributions of the CSB and LRC effects. Thus only the direct part of the Coulomb contribution to the energy should be included in the calculation, see also subparagraph IIA in Ref. [1].

4 Results and discussion

After performing the fit of the parameters for the two models with tensor couplings, various quantities for nuclei, nuclear matter and neutron stars can be calculated and compared to experimental data. Before they are presented, in the following subsections, a discussion of the model parameters and of the obtained density dependence of the coupling functions is of interest since they are essential to obtaining a good quality fit.

The parameters of the three relativistic EDF models of the present work are specified in Table 3. For the DDT and DDTC parameterisations, uncertainties are given as determined with the method described in Subsection 3.3. For the DD2 model, these are not available because the parameter set does not correspond to a minimum of χ^2 with the present set of observables and model uncertainties. The most obvious differences are the large values of the tensor couplings $\Gamma_{T\omega}$, and $\Gamma_{T\rho}$, and the small σ meson masses M_σ as compared to the value of the DD2 model without tensor couplings. This is not surprising since $\Gamma_{T\omega}$ and M_σ directly affect the description of the surface properties of nuclei and thus there is a strong correlation between them. The DD2 model is also characterized by a rather small saturation density. The isoscalar couplings $\Gamma_\sigma^{(0)}$ and $\Gamma_\omega^{(0)}$ at the reference density of the DDT and DDTC models are considerably smaller than those of the

Table 3 Parameters of the coupling functions, reference densities, and σ -meson masses for the different parameterisations of the relativistic EDF. Uncertainties of the quantities are given in brackets.

parameter	DDT		DDTC		DD2
$\Gamma_\sigma^{(0)}$	8.630588	(0.289206)	8.580686	(0.846337)	10.686681
a_σ	1.142684	(0.009581)	1.311104	(0.048916)	1.357630
b_σ	1.854752	(0.627900)	2.315517	(2.062872)	0.634442
c_σ	2.193260	(0.741533)	3.213878	(2.826693)	1.005358
d_σ	0.389847	(0.065899)	3.220510	(0.146240)	0.575810
$\Gamma_\omega^{(0)}$	11.14407	(0.29709)	11.09567	(0.86419)	13.342362
a_ω	2.891633	(1.032068)	1.434242	(0.204994)	1.369718
b_ω	1439.522	(1290.251)	9.292208	(10.52430)	0.496475
c_ω	4164.427	(5086.006)	13.65208	(17.02927)	0.817753
d_ω	0.008947	(0.005460)	0.156257	(0.097456)	0.638452
$\Gamma_\rho^{(0)}$	3.747188	(0.070045)	3.693565	(0.086777)	3.626940
a_ρ	0.684812	(0.050891)	0.675146	(0.054904)	0.518903
$\Gamma_{T\omega}$	3.200838	(0.621091)	3.489206	(1.881621)	0.000000
$\Gamma_{T\rho}$	18.67809	(3.74586)	20.50426	(3.39598)	0.000000
$\rho_{\text{ref}} [\text{fm}^{-3}]$	0.15493496	(0.00075982)	0.15304168	(0.00094838)	0.149065
$M_\sigma [\text{MeV}]$	511.9820	(6.5387)	510.5184	(19.2068)	546.2125

DD2 model. On the other hand, the couplings $\Gamma_\rho^{(0)}$ and the coefficient a_ρ are larger. Particularly striking are the large coefficients b_ω and c_ω with a small d_ω for the DDT model. This will lead to an unusual density dependence of the coupling Γ_ω , see below.

The correlations coefficients of the fit parameters in the DDT model are given in Figure 1 where boxes in red color indicate the largest absolute values whereas grey boxes correspond to the

	M_σ	M_{nuc}^*	n_{sat}	B_{sat}	J	K	L	r_{10}	r_{21}	$\Gamma_{T\omega}$	$\Gamma_{T\rho}$
M_σ	1.00	-0.95	-0.47	-0.55	0.08	0.65	0.42	-0.66	0.53	-0.98	0.03
M_{nuc}^*	-0.95	1.00	0.34	0.48	-0.19	-0.67	-0.47	0.58	-0.42	0.98	-0.07
n_{sat}	-0.47	0.34	1.00	0.30	-0.17	-0.34	-0.44	0.45	-0.44	0.38	0.29
B_{sat}	-0.55	0.48	0.30	1.00	0.48	-0.02	0.19	0.49	-0.40	0.47	-0.12
J	0.08	-0.19	-0.17	0.48	1.00	0.15	0.87	-0.14	0.08	-0.15	-0.04
K	0.65	-0.67	-0.34	-0.02	0.15	1.00	0.33	0.04	-0.13	-0.69	0.00
L	0.42	-0.47	-0.44	0.19	0.87	0.33	1.00	-0.40	0.30	-0.45	-0.28
r_{10}	-0.66	0.58	0.45	0.49	-0.14	0.04	-0.40	1.00	-0.96	0.59	0.05
r_{21}	0.53	-0.42	-0.44	-0.40	0.08	-0.13	0.30	-0.96	1.00	-0.43	-0.06
$\Gamma_{T\omega}$	-0.98	0.98	0.38	-0.47	-0.15	-0.69	-0.45	0.59	-0.43	1.00	-0.05
$\Gamma_{T\rho}$	0.03	-0.07	0.29	-0.12	-0.04	0.00	-0.28	0.05	-0.06	-0.05	1.00

Fig. 1 Correlation matrix of the fit parameters in the DDT model.

smallest moduli of the coefficients. As expected, a first group with M_σ , M_{nuc}^* , and $\Gamma_{T\omega}$ shows strong correlations since they all affect the description of the nuclear surface. In contrast, $\Gamma_{T\rho}$ is hardly correlated to any other parameter of the fit. The other two parameters related to the isovector part of the interaction, J , and L , however, show a strong correlation. Apart from this dependence, J seems to be practically uncorrelated to all other fit parameters. Another pair of parameters, r_{10} , and r_{21} , determines the density dependence of the isoscalar couplings. They are also strongly correlated. A somewhat lesser strength of correlation is found for the incompressibility coefficient K , and r_{10} with the first group of parameters.

The coupling functions $\Gamma_i(n_b)$ generally decrease with increasing baryon density n_b , see Figure 2. They approach a finite value in the high-density limit by construction, and go to zero for Γ_ρ , in particular. The isoscalar couplings for the models with tensor couplings (DDT, and DDTC) are significantly smaller than those of the model without tensor couplings (DD2). This can also be observed for the absolute values of the couplings at the reference density in Table 3. The strong rise of the ω meson coupling in the DDT model towards very small densities is particularly noteworthy. This behavior is a consequence of the large values of the parameters b_ω and c_ω in combination with a small d_ω . The isoscalar couplings, Γ_ω and Γ_σ , of the DDTC parameterisation have a much larger uncertainty as compared to those of the DDT model, but their shape is very similar to the corresponding couplings of the DD2 model. The density dependence of the ρ meson couplings is very similar for all models with slightly higher values for the models with tensor couplings.

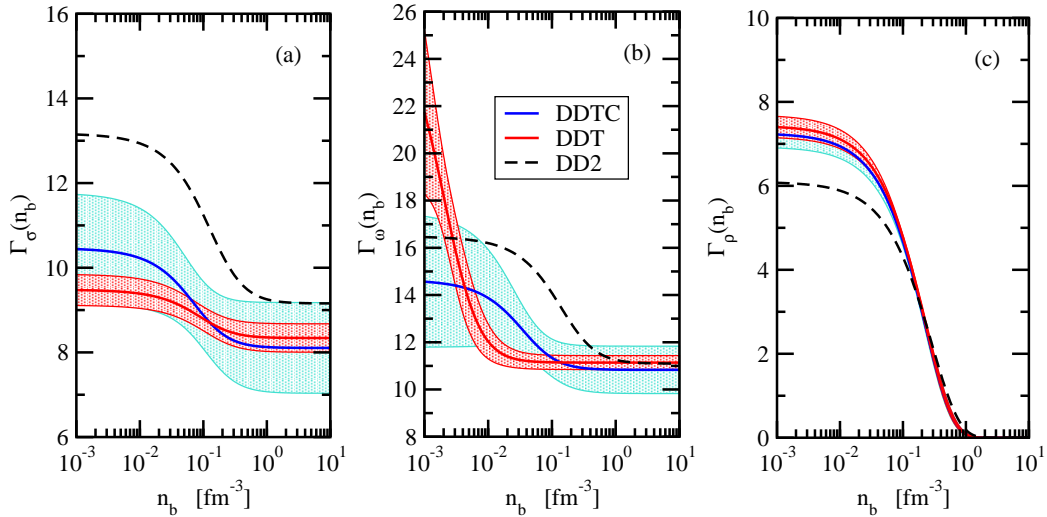


Fig. 2 Coupling functions $\Gamma_i(n_b)$ of the (a) σ meson, (b) ω meson, and (c) ρ meson for the different parameterisations of the relativistic EDF with uncertainty bands for DDTC and DDT.

Table 4 Fit uncertainties $\Delta\mathcal{O}_i^{(\text{fit})}$ of the observables \mathcal{O}_i for DDT.

observable \mathcal{O}_i	B [MeV]	r_c [fm]	r_d [fm]	σ [fm]	r_n [fm]	ΔE_{so} [MeV]	E_{mono} [MeV]
fit uncertainty $\Delta\mathcal{O}_i^{(\text{fit})}$	0.619311	0.013364	0.017155	0.026851	0.008249	0.240832	0.430714

4.1 Nuclei

Before analyzing the predictions of individual properties of finite nuclei, it is worthwhile to look at the fit uncertainties of the observables, see Table 4, and their contributions to the χ^2 function that are collected in Table 5 for the three parameterisations. The uncertainties of the energy quantities, i.e., the binding energy, the spin-orbit splitting, and the constraint isocalar monopole giant resonance energy, are all on a sub-MeV level, whereas the uncertainties of the size quantities, i.e., radii and skin thickness, are typically in the order of a few hundredths of a fm with the error in the root-mean-square (rms) valence neutron radius being the smallest. These results give an impression on the actual quality a description of nuclei with a relativistic EDF can achieve and how reasonable values have to be chosen in other attempts to find parameters of such models from fits to finite nuclei.

A comparison of the total χ^2 , see Table 5, and the contributions for the three models reveals interesting differences. First of all, it is evident that the DDT model gives the best description of the data with the lowest total χ^2 . By construction, its value is given by the number of degrees of freedom $N_{\text{dof}} = 39$. The other parameterisations, in particular the one without tensor couplings, are considerably worse. In case of the DDTC parameterisation this is mostly caused by the larger errors in the binding energies and the spin-orbit splittings. The values of χ^2 of the DD2 model is completely dominated by the difference of the valence neutron radii from the experimental values. Even neglecting their contribution to χ^2 , the description of experimental data with the DD2 model is almost always much worse than that of the DDT and DDTC models. All observables that are determined strongly by the surface description of a nucleus, viz., the radii, the skin thickness, and

Table 5 Contributions $\chi_i^2(\{p_k\})$ of the different observables and total $\chi^2(\{p_k\})$ for the different parameterisations of the relativistic EDF. The bottom line gives the sum of the quantities in the same column above.

observable i	$N_i^{(\text{obs})}$	DDT	DDTC	DD2
$B(Z, N)$	16	12.48	31.79	100.02
r_c	8	6.24	12.61	16.06
r_d	5	3.90	6.30	26.27
σ	5	3.90	5.08	2.24
r_n	2	1.56	4.01	578.17
ΔE_{so}	10	7.80	11.90	40.66
E_{mono}	4	3.12	2.86	3.61
	50	39.00	70.11	767.01

Table 6 Binding energies $B(Z, N)$ of nuclei in MeV from experiment [23] in comparison to theoretical values from different parameterisations of the relativistic EDF. Uncertainties of the quantities are given in brackets. The bottom line gives the root-mean-square deviation of the theoretical predictions from the experiment in MeV.

nucleus	experiment	DDT		DDTC		DD2
^{16}O	127.619	128.193	(0.262)	128.469	(0.285)	127.947
^{24}O	168.952	168.368	(0.327)	167.890	(0.440)	169.130
^{28}O	167.664	167.888	(0.701)	167.672	(0.839)	173.005
^{34}Si	283.464	284.471	(0.300)	283.732	(0.300)	284.044
^{34}Ca	243.882	244.060	(0.234)	245.259	(0.259)	246.245
^{40}Ca	342.052	342.161	(0.362)	342.366	(0.444)	342.203
^{48}Ca	416.001	416.545	(0.224)	416.225	(0.265)	414.929
^{48}Ni	347.328	346.740	(0.290)	348.870	(0.347)	350.092
^{56}Ni	483.996	483.435	(0.380)	483.523	(0.412)	482.346
^{68}Ni	590.408	589.675	(0.374)	588.546	(0.367)	590.595
^{78}Ni	642.564	642.398	(0.470)	642.460	(0.464)	642.048
^{90}Zr	783.897	782.939	(0.321)	782.332	(0.376)	780.727
^{100}Sn	825.163	825.984	(0.490)	825.978	(0.551)	826.231
^{132}Sn	1102.843	1103.173	(0.394)	1103.256	(0.456)	1103.388
^{140}Ce	1172.683	1172.895	(0.423)	1173.098	(0.625)	1172.814
^{208}Pb	1636.430	1636.354	(0.531)	1636.477	(0.530)	1635.922
		0.562		0.919		1.907

the spin-orbit splitting, are on the average better described in the EDFs with tensor couplings. Only the surface thickness σ is slightly better described by the DD2 model.

The first quantity of major interest is the binding energy $B(Z, N)$ of a nucleus that is predicted by a given parameterisation of a relativistic EDF. The results of the binding energy calculations of the three models of the present work are listed in Table 6, for nuclei considered in the fit, in comparison to experimental values from the Atomic Mass Evaluation 2020 [23]. In order to have a better impression of the quality of the models, the differences between the experimental and theoretical data are depicted in Figure 3. It is seen that the models with tensor coupling show less

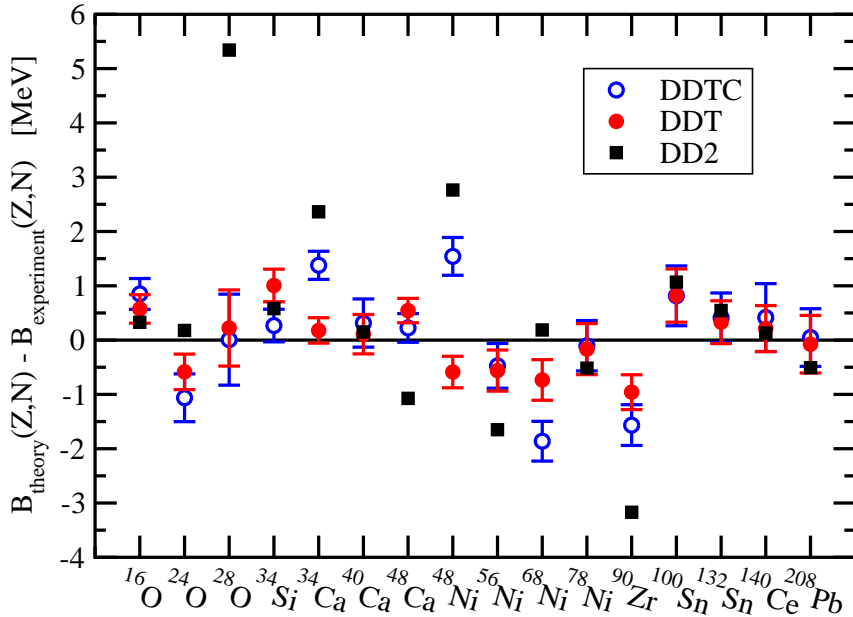


Fig. 3 Binding energy differences $B_{\text{theory}}(Z, N) - B_{\text{experiment}}(Z, N)$ of nuclei used in the parameter fits with theoretical uncertainties indicated by the error bars.

fluctuations and deviate on the average less strongly from the experimental data than the models without tensor couplings. This is also reflected in the root-mean-square deviation of the theoretical values from the experimental data in the bottom line of Table 6. The trend of these numbers agrees with the variation of the binding energy contribution to the total χ^2 shown in Table 5.

Also interesting observations for individual sets of nuclei can be made. In contrast to the DD2 parameterisation, the binding energy of ^{28}O is smaller than that of ^{24}O in the DDT and DDTC parameterisations, a result that is difficult to achieve in most other relativistic EDFs. Similar patterns can be seen in Figure 3 when comparing different parameterisations, e.g., for the heaviest nuclei. There are also striking effects for the set of Ni nuclei with different trends when comparing the models. It is seen in Table 6 that the calculated binding energies of ^{48}Ni obtained for the DDT model without the $(Z - 1)/Z$ factor is significantly closer to the experimental value than that of the DDTC and DD2 models with the $(Z - 1)/Z$ factor.

Theoretical values of the quantities related to the charge form factor are given in Table 7 in comparison to experimental data for the nuclei in the fit. The theoretical uncertainties are generally in the order of 0.005 fm. Differences between theory and experiment are depicted in Figure 4 with three panels for the charge radius, the diffraction radius, and the surface thickness. There is a good agreement with typical differences between theory and experiment of less than 0.02 fm, and a clear trend in the deviations is not seen. Only the surface thickness of ^{90}Zr is overestimated by more than 0.04 fm. The values of the valence neutron radii of ^{17}O and ^{41}Ca can also be found in Table 7. The deviations between theory and experiment are slightly larger than those of the

Table 7 Experimental data of charge radii, diffraction radii, surface thicknesses [24–27] and valence neutron radii [28, 29] in fm of nuclei used in the fit, in comparison to theoretical values from different parameterisations of the relativistic EDF. Uncertainties of the quantities are given in brackets.

	nucleus	experiment	DDT	DDTC	DD2
charge radius r_d	^{16}O	2.699	2.705 (0.005)	2.689 (0.011)	2.691
	^{40}Ca	3.478	3.453 (0.003)	3.440 (0.004)	3.463
	^{48}Ca	3.477	3.489 (0.005)	3.482 (0.007)	3.478
	^{68}Ni	3.887	3.871 (0.004)	3.864 (0.004)	3.887
	^{90}Zr	4.269	4.269 (0.004)	4.264 (0.004)	4.282
	^{132}Sn	4.709	4.707 (0.005)	4.708 (0.005)	4.732
	^{140}Ce	4.877	4.886 (0.005)	4.888 (0.005)	4.897
	^{208}Pb	5.501	5.504 (0.006)	5.507 (0.008)	5.540
diffraction radius r_d	^{16}O	2.764	2.767 (0.006)	2.756 (0.011)	2.707
	^{40}Ca	3.849	3.832 (0.004)	3.825 (0.005)	3.816
	^{48}Ca	3.963	3.973 (0.005)	3.971 (0.010)	3.953
	^{90}Zr	5.040	5.015 (0.005)	5.015 (0.006)	5.019
	^{208}Pb	6.776	6.787 (0.008)	6.799 (0.009)	6.829
	surface thickness σ	^{16}O	0.851	0.828 (0.005)	0.810 (0.008)
^{40}Ca		0.968	0.964 (0.005)	0.946 (0.009)	0.968
^{48}Ca		0.890	0.909 (0.005)	0.899 (0.006)	0.897
^{90}Zr		0.957	1.001 (0.005)	0.993 (0.007)	0.994
^{208}Pb		0.919	0.914 (0.004)	0.906 (0.006)	0.912
valence neutron radius r_n	^{17}O	3.360	3.356 (0.008)	3.377 (0.008)	3.514
	^{41}Ca	3.990	3.999 (0.006)	3.990 (0.011)	4.116

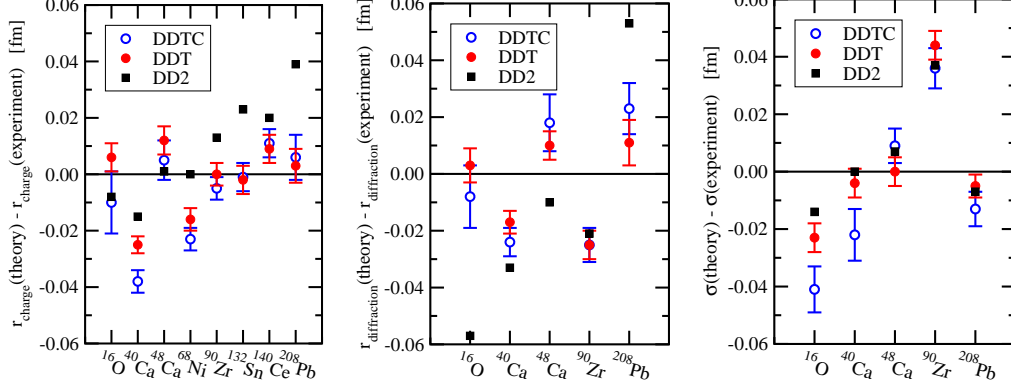


Fig. 4 Differences between theoretical and experimental charge radii r_c , diffraction radii r_d and surface thicknesses σ , respectively, of nuclei used in the fit of the model parameters. Theoretical uncertainties are indicated by the error bars.

quantities related to the charge form factor, but the agreement with the experimental data is still satisfactory, given the large theoretical uncertainties.

The differences between experimental and theoretical values of the spin-orbit splittings can be explored by studying Table 8. Considering the theoretical uncertainties of somewhat less than 0.1 MeV, there is a fair agreement of these data. The difference between the experimental spin-orbit splittings of the $\nu 0p$ and $\pi 0p$ levels in ^{16}O (-0.140 MeV) is not reproduced by the theoretical models as their differences are positive, 0.182 MeV and 0.170 MeV for the DDT and DDTC models, respectively. The spin-orbit splitting of the $\nu 0p$ levels is larger than that of the $\pi 0p$ levels in contrast to the experiment, in particular for the DD2 parameterisation. The spin-orbit splittings of the $\nu 1p$ levels in ^{48}Ca are underestimated in the theoretical models in comparison to the experimental value. Larger differences between theory and experiment are also observed for the $\pi 1d$ levels in ^{132}Sn , and ^{208}Pb . In general, the results of the DD2 model show a larger deviation from the experiment as compared to the models with tensor couplings.

Table 8 Experimental data of spin-orbit splittings [30, 31] in MeV of single-particle levels in nuclei used in the fit in comparison to theoretical values from different parameterisations of the relativistic EDF. Uncertainties of the quantities are given in brackets.

nucleus	level	experiment	DDT	DDTC	DD2
^{16}O	$\nu 0p$	6.180	6.127 (0.095)	6.231 (0.214)	6.867
	$\pi 0p$	6.320	5.945 (0.094)	6.061 (0.209)	6.819
^{48}Ca	$\nu 1p$	2.020	1.841 (0.068)	1.849 (0.075)	1.510
^{90}Zr	$\pi 1p$	1.510	1.598 (0.049)	1.649 (0.121)	1.701
^{132}Sn	$\pi 1d$	1.480	1.749 (0.080)	1.825 (0.202)	2.014
	$\pi 0g$	6.140	6.254 (0.097)	6.083 (0.169)	6.720
^{140}Ce	$\nu 2p$	0.475	0.560 (0.068)	0.622 (0.049)	0.517
^{208}Pb	$\nu 2p$	0.898	1.066 (0.065)	0.993 (0.037)	0.930
	$\pi 1d$	1.330	1.680 (0.037)	1.732 (0.064)	1.868
	$\pi 0h$	5.550	5.712 (0.088)	5.527 (0.085)	6.203

Table 9 Experimental data of constraint isoscalar monopole giant resonance energies [32] in MeV of nuclei used in the fit in comparison to theoretical values from different parameterisations of the relativistic EDF. Uncertainties of the quantities are given in brackets.

nucleus	experiment	DDT		DDTC		DD2
⁹⁰ Zr	17.810	17.597	(0.214)	17.714	(0.214)	17.584
¹¹⁶ Sn	15.900	16.112	(0.193)	16.189	(0.196)	16.085
¹⁴⁴ Sm	15.250	15.158	(0.212)	15.220	(0.318)	15.205
²⁰⁸ Pb	14.180	13.489	(0.188)	13.519	(0.232)	13.417

The energies of the isoscalar monopole giant resonance are crucial, in the fit of the model parameters, to obtain a reasonable value of the incompressibility coefficient K of nuclear matter. Experimental data and theoretical values are given in Table 9 with theoretical uncertainties in the order of 0.2 MeV. In general, there is a good reproduction of the experimental values by theory, by the models with and without tensor couplings. Only the prediction for the resonance energy of ²⁰⁸Pb is on the lower side as compared to the experiment.

In the determination of the model parameters, several exotic nuclei on both sides of the valley of stability were included in order to better constrain the isovector part of the effective in-medium interaction. In contrast to most earlier relativistic EDFs with density dependent couplings, three independent isovector parameters are considered in the parameterisations that include tensor couplings. It is interesting to study, how this affects the predictions of the neutron skin thickness of nuclei, $\Delta r_{\text{skin}} = r_{\nu} - r_{\pi}$, that is obtained by the difference between the neutron and proton rms radii. The theoretical values for the nuclei in the fit are collected in Table 10. Nuclei with $N = Z$ exhibit a small negative value of Δr_{skin} that becomes even more negative for neutron deficient nuclei like ³⁴Ca and ⁴⁸Ni. On the other hand, neutron-rich nuclei can develop a substantial neutron skin. This

Table 10 Theoretical neutron skin thickness Δr_{skin} in fm of selected nuclei used in the fit from different parameterisations of the relativistic EDF. Uncertainties of the quantities are given in brackets.

nucleus	DDT		DDTC		DD2
¹⁶ O	-0.031	(0.001)	-0.029	(0.001)	-0.029
²⁴ O	0.450	(0.014)	0.480	(0.018)	0.595
²⁸ O	0.622	(0.019)	0.650	(0.042)	0.769
³⁴ Si	0.181	(0.007)	0.183	(0.007)	0.203
³⁴ Ca	-0.299	(0.007)	-0.302	(0.008)	-0.323
⁴⁰ Ca	-0.053	(0.001)	-0.052	(0.001)	-0.053
⁴⁸ Ca	0.125	(0.008)	0.127	(0.008)	0.191
⁴⁸ Ni	-0.251	(0.007)	-0.251	(0.006)	-0.316
⁵⁶ Ni	-0.057	(0.001)	-0.057	(0.001)	-0.054
⁶⁸ Ni	0.166	(0.008)	0.167	(0.009)	0.200
⁷⁸ Ni	0.251	(0.012)	0.249	(0.013)	0.329
⁹⁰ Zr	0.040	(0.007)	0.039	(0.007)	0.083
¹⁰⁰ Sn	-0.083	(0.001)	-0.083	(0.001)	-0.082
¹³² Sn	0.191	(0.011)	0.189	(0.013)	0.261
¹⁴⁰ Ce	0.086	(0.009)	0.083	(0.010)	0.150
²⁰⁸ Pb	0.134	(0.010)	0.130	(0.013)	0.198

is most clearly seen for ^{24}O , ^{28}O , ^{78}Ni , and ^{132}Sn . The theoretical uncertainties, however, become much larger for the most exotic nuclei as compared to stable nuclei. The neutron skin thicknesses of more exotic nuclei are generally larger for the DD2 models as compared to the DDT and DDTC models. Also stable nuclei such as ^{48}Ca and ^{208}Pb show a sizeable neutron skin thickness. It can be determined experimentally by studying the parity-violation asymmetry in high-energy electron scattering experiments. A comparison of the theoretical predictions in Table 10 with the experimental data of the CREX experiment [38] with $\Delta r_{\text{skin}}(^{48}\text{Ca}) = 0.121 \pm 0.025$ (exp.) ± 0.024 (model) fm and those of the combined PREX experiments [39] with $\Delta r_{\text{skin}}(^{208}\text{Pb}) = 0.283 \pm 0.071$ fm shows that the theory can nicely reproduce the size of the neutron skin in ^{48}Ca within the uncertainties but it predicts a considerably smaller neutron skin thickness in ^{208}Pb , an issue that is not solved so far. The neutron skin thickness can also be determined using hadronic probes using precisely known proton radii from electron scattering. A former analysis of 1 GeV proton scattering on ^{48}Ca [40] gave a neutron skin thickness of $\Delta r_{\text{skin}} = 0.10 \pm 0.03$ fm only slightly smaller but consistent within the errors with the CREX result. A more recent study of neutron radii using proton scattering [41] gave ranges of $0.056 \text{ fm} < \Delta r_{\text{skin}}(^{48}\text{Ca}) < 0.102 \text{ fm}$ and $0.083 \text{ fm} < \Delta r_{\text{skin}}(^{208}\text{Pb}) < 0.111 \text{ fm}$ that point to rather small neutron thicknesses of these nuclei.

The inclusion of pairs of mirror nuclei in the fit also allows to better constrain the mirror displacement energies. The binding energy differences of three pairs of mirror nuclei are given in Table 11. There is a good agreement between experiment and theory with theoretical results of the DDT model that are somewhat larger than the experimental values. The differences between experimental and theoretical values are 0.374, 0.883, and 1.132 MeV for the pairs with mass number $A = 41$, 34, and 48 for the DDT model, respectively, thus overestimating the binding energy differences. In contrast, they are systematically smaller with 0.072, -1.055 , and -1.318 MeV for the DDTC model and -0.237 , -1.738 , and -3.836 MeV for the DD2 model, respectively, where the $Z(Z - 1)$ factor in the Coulomb field was introduced. In addition, the neutron-deficient nuclei were not considered in the fit of the parameters in the latter parameterisation. Thus the parameter set DDT gives the best description on the average. The theoretical uncertainties increase with the isospin difference of the pair of nuclei.

Table 11 Experimental binding energy differences in MeV of mirror nuclei in comparison to theoretical values from different parameterisations of the relativistic EDF. Uncertainties of the quantities are given in brackets.

pair of mirror nuclei	experiment	DDT		DDTC		DD2
$^{41}\text{Ca} - ^{41}\text{Sc}$	7.278	7.652	(0.031)	7.350	(0.030)	7.041
$^{34}\text{Si} - ^{34}\text{Ca}$	39.528	40.411	(0.170)	38.473	(0.168)	37.790
$^{48}\text{Ca} - ^{48}\text{Ni}$	68.673	69.805	(0.272)	67.355	(0.244)	64.837

4.2 Nuclear matter

The energy per nucleon E/A , Eq. (58), in homogeneous nuclear matter is a function of the baryon density $n_b = n_\nu + n_\pi$ and the isospin asymmetry $\alpha = (n_\nu - n_\pi)/n_b$. For $\alpha = 0$, the energy per nucleon of symmetric nuclear matter $E_0 = E/A(n_b, 0)$ is obtained. It is depicted in Figure 5 for the parameterisations DDT, DDTC, and DD2. The minimum of E_0 for these equations of state defines the saturation density n_{sat} , see Table 12. The region of negative slope, i.e., negative pressure, signals an instability of homogeneous matter that is related to the occurrence of the liquid-gas phase transition. At high densities, the predictions for the energy per nucleon become less certain as the widening of the uncertainty bands of the DDT and, significantly larger, DDTC models shows. The energy per nucleon of pure neutron matter, i.e., E/A for $\alpha = 1$, is also shown in Figure 5. It increases monotonically with the baryon density.

The curves of the DDT and DD2 parameterisations in Fig. 5 look very similar at first sight. But there are differences in detail, in particular at lower densities. The curves of the parameterisation DDTC follow along the lower limit of the uncertainty bands of the DDT model, hence signaling a softer equation of state. The neutron matter equation of state of the DDT model shows a peculiar feature at the lowest densities. This can be seen in the inset of Figure 5. The energy per nucleon

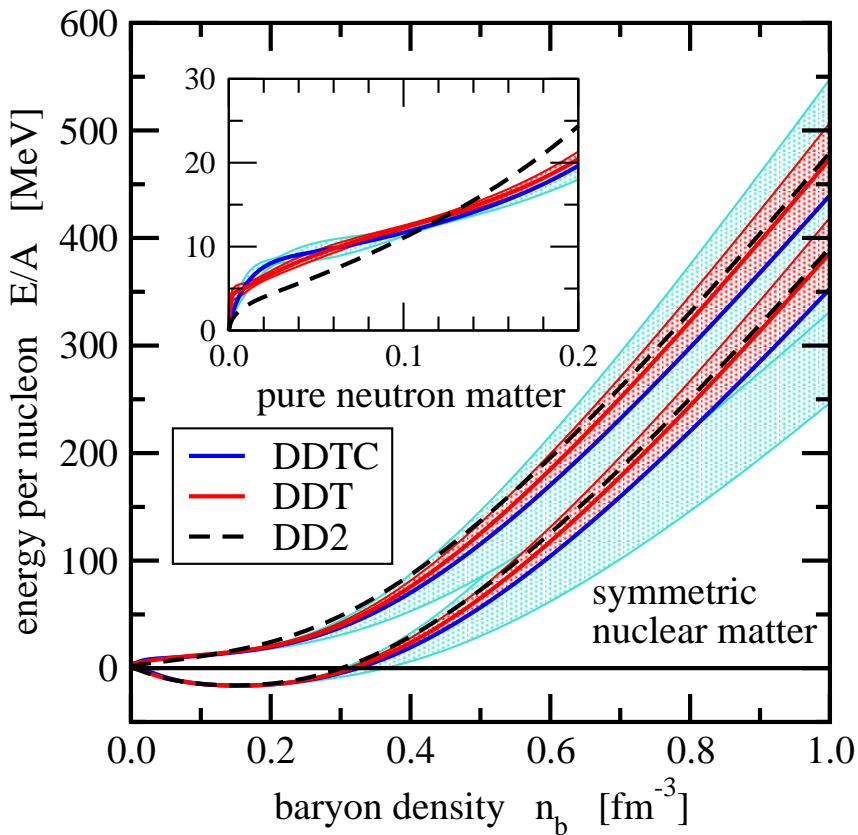


Fig. 5 Equation of state of symmetric nuclear matter and pure neutron matter, respectively, with theoretical uncertainty bands for the DDT and DDTC models. The inset shows the low-energy equation of state of pure neutron matter.

does not approach zero as smoothly as in the DD2 and DDTC models. This is related to the specific density dependence of the ω -meson coupling Γ_ω , see panel (b) of Figure 2. The increase of the coupling at very small densities causes an additional repulsion, which also applies for symmetric nuclear matter at very low densities (not shown in the inset).

Assuming a quadratic dependence of E/A on α for given baryon density n_b , the symmetry energy (59) can be obtained as a difference $E_{\text{sym}}(n_b) = E/A(n_b, 1) - E/A(n_b, 0)$. This quantity is shown in Figure 6 as function of n_b . Particularly noteworthy is the change of the slope above saturation density, for the DDT and DDTC models, with a widening of the uncertainty bands. At densities below saturation, symmetry energy is well constrained by experiments and ab-initio calculations of pure neutron matter, see, e.g., Refs. [42, 43] and references therein. At densities above saturation, the predictions for the equation of state of nuclear matter are less precise as indicated by the increasing uncertainty bands.

The E_{sym} curves of the DDT, DDTC, and DD2 model cross at a density below n_{sat} . It has been observed before that fitting model parameters of EDFs to properties of nuclei effectively determines the symmetry energy around this subsaturation density, see, e.g., Ref. [44]. A comparison of the low-density symmetry energy of the DDT, DDTC, and DD2 models with experimental data is depicted

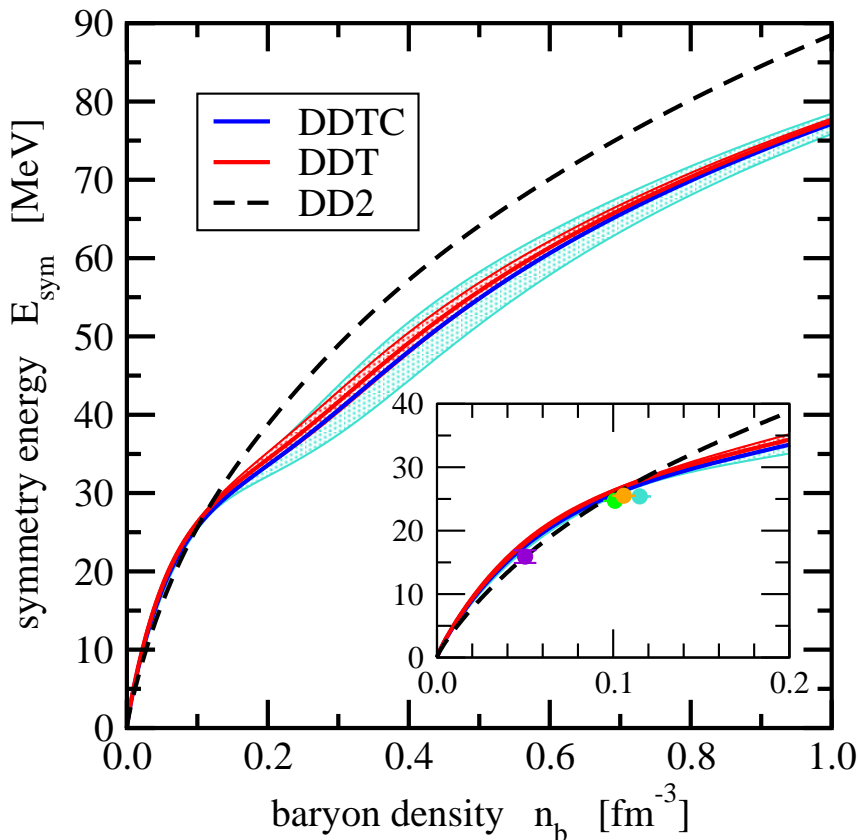


Fig. 6 Symmetry energy E_{sym} as function of the baryon density n_b with theoretical uncertainty bands for the DDT and DDTC models. The inset shows the low density part with a comparison to experimental data, see text for details.

in the inset of Figure 6. These data come from the determination of the dipole polarizability of ^{208}Pb (violet), the analysis of EDFs (green, light blue), and isobaric analog states (orange), see Ref. [45] and references therein. The symmetry energy of the parameterisations DDT and DDTC lie slightly above these points, corresponding to the small slope parameter L , whereas the DD2 curve matches the data somewhat better.

The energy per nucleon of symmetric matter near saturation can be expanded as

$$E_0(n_b) = -B_{\text{sat}} + \frac{1}{2}Kx^2 + \frac{1}{6}Qx^3 + \dots, \quad (91)$$

with $x = (n_b - n_{\text{sat}})/(3n_{\text{sat}})$ without a term linear in x because the pressure at saturation is $p(n_{\text{sat}}) = 0$. The incompressibility coefficient

$$K = 9n_{\text{sat}}^2 \left. \frac{d^2}{d(n_b)^2} E_0 \right|_{n_{\text{sat}}} = 9 \left. \frac{dp}{dn_b} \right|_{n_{\text{sat}}}, \quad (92)$$

and skewness parameter

$$Q = 27n_{\text{sat}}^3 \left. \frac{d^3}{d(n_b)^3} E_0 \right|_{n_{\text{sat}}}, \quad (93)$$

are found as second and third derivatives of E_0 . Similarly, the symmetry energy can be written as

$$E_{\text{sym}}(n_b) = J + Lx + \frac{1}{2}K_{\text{sym}}x^2 + \dots, \quad (94)$$

with the symmetry energy at saturation $J = E_{\text{sym}}(n_{\text{sat}})$, the slope parameter

$$L = 3n_{\text{sat}} \left. \frac{dE_{\text{sym}}}{dn_b} \right|_{n_{\text{sat}}}, \quad (95)$$

and the symmetry incompressibility

$$K_{\text{sym}} = 9n_{\text{sat}}^2 \left. \frac{d^2 E_{\text{sym}}}{d(n_b)^2} \right|_{n_{\text{sat}}}. \quad (96)$$

It is also useful to define the so-called volume part of the isospin compressibility

$$K_{\tau,v} = K_{\text{sym}} - 6L - \frac{QL}{K}, \quad (97)$$

that describes the change of the incompressibility with the variation in α [15, 46]. These quantities, together with the effective Dirac mass at saturation $(M_{\text{nuc}}^*)_{\text{sat}} = M_{\text{nuc}} - C_{\sigma}n_{\text{sat}}^{(s)}$, are convenient

Table 12 Characteristic nuclear matter parameters for different parameterisations of the relativistic EDF. Uncertainties of the quantities are given in brackets.

quantity	unit	DDT		DDTC		DD2
n_{sat}	fm^{-3}	0.15493	(0.00076)	0.15304	(0.00095)	0.14907
$(M_{\text{nuc}}^*)_{\text{sat}}$	M_{nuc}	0.65729	(0.01315)	0.66305	(0.03803)	0.56252
B_{sat}	MeV	16.226	(0.025)	16.226	(0.040)	16.022
K	MeV	229.20	(7.99)	215.05	(7.71)	242.72
Q	MeV	88.565	(230.061)	-291.86	(763.87)	168.77
J	MeV	31.209	(0.498)	30.379	(0.568)	31.670
L	MeV	34.236	(4.332)	33.317	(7.847)	55.033
K_{sym}	MeV	-69.538	(15.454)	-75.562	(26.416)	-93.226
$K_{\tau,v}$	MeV	-288.18	(54.09)	-230.25	(131.21)	-461.69

to characterize the equation of state of nuclear matter around saturation. They are given in Table 12 for the models DDT, DDTC, and DD2. Most remarkable are the increased effective mass and the reduced incompressibility coefficient of the models with tensor couplings (DDT and DDTC) in comparison to that without these couplings (DD2). Most existing relativistic models show values of K that are rather high when compared with non-relativistic EDFs, cf. Refs. [3, 15]. The tensor models are an exception and they are also characterized by rather large saturation densities. The higher-order coefficients Q and K_{sym} show considerable differences and are not very well determined by the parameter fits as they have large uncertainties. The smaller values of K and Q of the DDTC model indicate a softer equation of state as compared to the DDT model as seen already in Figure 5. The DDT and DDTC models also have symmetry energy slope parameters that are smaller than the value of L of the DD2 model. This difference correlates with the smaller neutron skin thicknesses for exotic nuclei as discussed in Subsection 4.1.

4.3 Neutron stars

The properties of a non-rotating, spherically symmetric neutron star, are obtained by solving the first-order Tolman-Oppenheimer-Volkoff equation [54, 55]

$$\frac{dp}{dr} = -G \frac{M(r)\varepsilon(r)}{r^2} \left[1 + \frac{P(r)}{\varepsilon(r)} \right] \left[1 + \frac{4\pi r^3 P(r)}{M(r)} \right] \left[1 - \frac{2GM(r)}{r} \right]^{-1}, \quad (98)$$

with the mass

$$M(r) = 4\pi \int_0^r dr' (r')^2 \varepsilon(r'), \quad (99)$$

inside the volume of radius r . The factors in square brackets are the general relativistic corrections to the classical expression for the change of the pressure with the radius. Assuming a particular density n_{central} in the center of the star, the first order differential equation (98) can be solved by an outward integration until the pressure $P(r)$ becomes sufficiently small. This defines the stellar radius R and the total mass $M(R)$. The essential ingredient in the calculation is the equation of

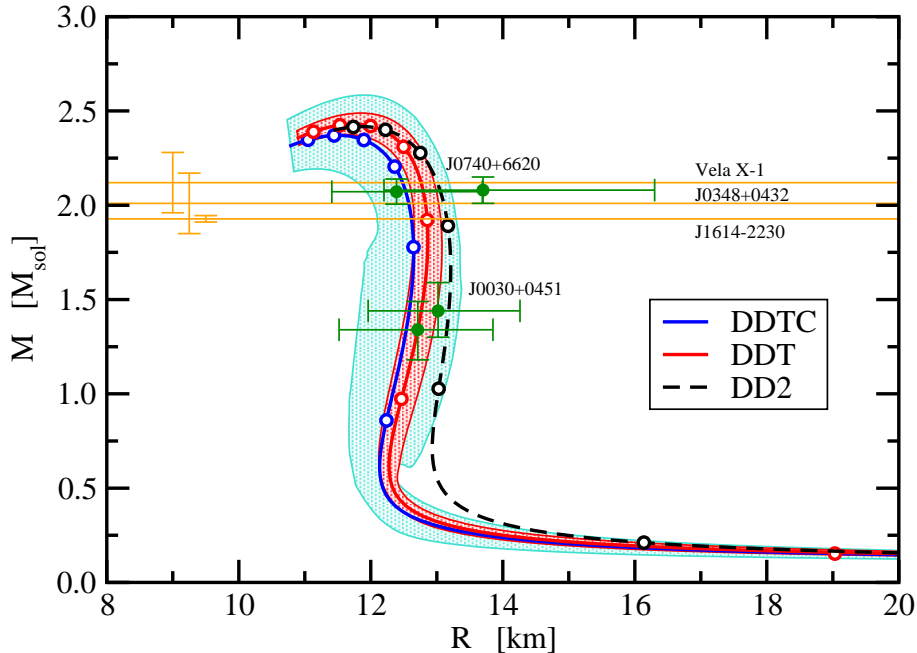


Fig. 7 Mass-radius relation of neutron stars for the parameterisations DDTC (blue), DDT (red), with uncertainty bands, and DD2 (black) of the relativistic EDF. Open circles indicate neutron stars where the central density is an integer multiple $n_{\text{central}} = kn_{\text{sat}}$ of the saturation density starting with $k = 1$ at the lowest masses. (The point with $k = 1$ of the DDTC parameterisation is at a radius $R = 21.62$ fm outside the figure.) Yellow lines give the masses of heavy neutron stars [47–49] with errors indicated on the left. Masses and radii of neutron stars from NICER observations [50–53] are shown in green color.

state of charge-neutral matter in β equilibrium. It is obtained by adding the leptonic contributions (electrons and muons) to the nuclear equation of state and determining the isospin asymmetry α for given baryon density n_b , by requiring vanishing lepton chemical potentials $\mu_e + \mu_q$, and $\mu_\mu + \mu_q$, with charge chemical potential $\mu_q = \mu_\pi - \mu_\nu$. At densities below nuclear saturation, an appropriate crust equation of state has to be used as the matter is no longer homogeneous. Here, the crust description of the generalized relativistic density functional with the DD2 parameterisation of the couplings [34] is used where the masses of the nuclei in the crust are taken from the Duflo-Zuker model DZ31 [56], if not available from the atomic mass evaluation AME2020 [23].

The mass-radius relations of neutron stars for the different parameterisations are depicted in Figure 7. Open circles on the curves denote the properties of neutron stars with central densities that are an integer multiple of the saturation density n_{sat} . The curves show the well-known inverse S-shaped rise of the mass with increasing central density and the corresponding variation of the radius. Ordinary neutron stars with masses of 1.4 times the solar mass M_{sol} have central densities that are typically between twice and three times the saturation density. At certain central densities $n_{\text{central}}^{(\text{max})}$, the most massive neutron star configurations are obtained. They have central densities of five to six times the saturation density. Neutron stars with higher central density are not stable any more and this last branch of the curve will not be populated. The maximum masses of the shown models are always above the largest masses of observed neutron stars [47–49] since their

Table 13 Properties of neutron stars for the different parameterisations of the relativistic EDF.

quantity	unit	DDT	DDTC	DD2
$R_{1.4}$	km	12.744	12.566	13.172
M_{\max}	M_{sol}	2.430	2.371	2.417
R_{\max}	km	11.739	11.504	11.869
$n_{\text{central}}^{(\max)}$	fm^{-3}	0.85785	0.89663	0.85114

equation of state is sufficiently stiff. Masses and radii are available from NICER observations [50–53], but these data have large uncertainties. All models are consistent with these observations. Characteristic properties of neutron stars of the models in this work are collected in Table 13. The properties of the maximum mass stars are very similar in all models but the radii of the DD2 model are systematically larger than those of the parameterisation DDT and DDTC. The latter model predicts the lowest maximum mass, a higher central density at this mass, and smaller radii as compared to the other models, corresponding to the softer equation of state.

5 Summary and Conclusions

In this work, an extension of a relativistic EDF is presented that includes tensor couplings between the Lorentz vector mesons, ω and ρ , and nucleons in addition to the standard minimal meson-nucleon couplings. The latter are assumed to depend on the baryon density. The field equations are derived in the mean-field approximation from a covariant Lagrangian density and solved self-consistently for nuclei and nuclear matter.

The parameters of this phenomenological approach are found from a fit to properties of 20 selected nuclei that comprise binding energies, charge and diffraction radii, surface thicknesses, spin-orbit splittings, valence neutron radii, and constraint isoscalar monopole giant resonance energies. The model uncertainties of these quantities are determined self-consistently during the fitting procedure. The model predictions are compared to experimental data and given with their theoretical uncertainties, which were, to our knowledge, not specified in earlier parameterisations of relativistic EDFs. Two new sets of parameters, DDT and DDTC, are developed that differ in the treatment of the Coulomb interaction.

The inclusion of tensor couplings in the relativistic EDF leads to a considerable improvement in the description of nuclear properties, in particular their binding energies. Quantities related to the nuclear charge form factor show a similar quality as those of an earlier parameterisation (DD2) without tensor couplings. The binding energy differences of mirror nuclei are also closer to the experimental data than in the DD2 model, that did not consider exotic, neutron deficient nuclei

in the determination of the parameters. Predictions for the neutron skin thickness of bound and unstable nuclei are made.

The equations of state for symmetric nuclear matter and pure neutron matter are calculated with the new parameters. They look similar as those of the DD2 model but show some specific differences. These are most apparent by comparing characteristic nuclear matter parameters. The new parameterisations exhibit larger saturation densities and effective nucleon masses, and smaller incompressibility coefficients and symmetry energy slope parameters.

The description of charge-neutral nuclear matter in β equilibrium with the extended EDFs allows to calculate properties of neutron stars and, in particular, their mass-radius relation. The results are similar as for the DD2 model but with slightly smaller radii. Due to the stiffness of the EOS at high densities, the maximum masses are predicted to lie above the data of observed heavy neutron stars. The obtained mass-radius relations are consistent with results from NICER measurements that still have substantial uncertainties, in particular for the radii.

The EDFs with the new parameterisations can be studied in the future for larger sets of nuclei, including deformed ones, taking other effects like pairing into account. The additional tensor couplings, however, require some extra work to be considered in such deformed calculations. The new models can also be used to prepare EOS tables of stellar matter at finite temperature for larger ranges in isospin asymmetry and density, in order to be used in simulations of core-collapse supernovae and neutron-star mergers [57]. For this, the calculations have to be extended by including additional degrees of freedom, e.g., light clusters at subsaturation densities [34, 58], or hyperons at high densities, see, e.g., Ref. [59].

Acknowledgments

S. Typel acknowledges the support by the Cyclotron Institute, Texas A&M University. S. Shlomo is partially supported by the US Department of Energy under Grant no. DE-FG03-93ER-40773.

Appendix A Transformation between parameters of nuclear matter and of coupling functions

The parameters of the coupling functions (60) can be derived from the characteristic nuclear matter parameters. To simplify this conversion, the average nucleon mass $M_{\text{nuc}} = (M_{\pi} + M_{\nu})/2$ is used instead of proton and neutron masses in the full calculation. However, this does not pose any problem.

1. The reference mass ϱ_{ref} is chosen as the baryon density at saturation n_{sat} and defines the Fermi momentum

$$k_{\text{sat}}^* = \left(\frac{3\pi^2}{2} n_{\text{sat}} \right)^{1/3}. \quad (\text{A1})$$

2. The Dirac effective mass at saturation M_{sat}^* gives the effective chemical potential

$$\mu_{\text{sat}}^* = \sqrt{(k_{\text{sat}}^*)^2 + (M_{\text{sat}}^*)^2}, \quad (\text{A2})$$

and the scalar density at saturation

$$n_{\text{sat}}^{(s)} = \frac{M_{\text{sat}}^*}{\pi^2} \left[k_{\text{sat}}^* \mu_{\text{sat}}^* - (M_{\text{sat}}^*)^2 \ln \left(\frac{k_{\text{sat}}^* + \mu_{\text{sat}}^*}{M_{\text{sat}}^*} \right) \right]. \quad (\text{A3})$$

This determines the scalar coupling at saturation

$$C_\sigma = \frac{M_{\text{nuc}} - M_{\text{sat}}^*}{n_{\text{sat}}^{(s)}}, \quad (\text{A4})$$

and the auxiliary quantity

$$f_{\text{sat}} = 3 \left(\frac{n_{\text{sat}}^{(s)}}{M_{\text{sat}}^*} - \frac{n_{\text{sat}}}{\mu_{\text{sat}}^*} \right), \quad (\text{A5})$$

that will be used below.

3. The energy per nucleon at saturation $(E/A)_{\text{sat}}$ gives the energy density at saturation

$$\varepsilon_{\text{sat}} = [(E/A)_{\text{sat}} + M_{\text{nuc}}] n_{\text{sat}}, \quad (\text{A6})$$

and the vector coupling at saturation

$$C_\omega = \frac{2}{n_{\text{sat}}^2} \left[\varepsilon_{\text{sat}} - \frac{1}{4} \left(3\mu_{\text{sat}}^* n_{\text{sat}} + M_{\text{sat}}^* n_{\text{sat}}^{(s)} \right) - \frac{1}{2} C_\sigma \left(n_{\text{sat}}^{(s)} \right)^2 \right]. \quad (\text{A7})$$

Furthermore, the chemical potential

$$\mu_{\text{sat}} = \frac{\varepsilon_{\text{sat}}}{n_{\text{sat}}} = (E/A)_{\text{sat}} + M_{\text{sat}}, \quad (\text{A8})$$

and the rearrangement potential

$$V^{(R)} = \mu_{\text{sat}} - \mu_{\text{sat}}^* - C_\omega n_{\text{sat}}, \quad (\text{A9})$$

are found.

4. The ratio r_{10} determines the derivatives

$$C'_\omega = 2r_{10} \frac{C_\omega}{n_{\text{sat}}}, \quad (\text{A10})$$

and

$$C'_\sigma = \frac{1}{\left(n_{\text{sat}}^{(s)}\right)^2} \left(C'_\omega n_{\text{sat}}^2 - 2V^{(R)} \right), \quad (\text{A11})$$

at saturation. Then, the second and third auxiliary variables

$$g_{\text{sat}} = \frac{\frac{M_{\text{sat}}^*}{\mu_{\text{sat}}^*} - C'_\sigma n_{\text{sat}}^{(s)} f_{\text{sat}}}{1 + C_\sigma f_{\text{sat}}}, \quad (\text{A12})$$

and,

$$h_{\text{sat}} = -\frac{C'_\sigma n_{\text{sat}}^{(s)} + C_\sigma \frac{M_{\text{sat}}^*}{\mu_{\text{sat}}^*}}{1 + C_\sigma f_{\text{sat}}}, \quad (\text{A13})$$

can be calculated.

5. The ratio r_{21} is used to obtain the second derivative

$$C''_\omega = 2r_{10}(r_{10} + r_{21}) \frac{C_\omega}{n_{\text{sat}}^2}, \quad (\text{A14})$$

for the ω meson at saturation.

6. The incompressibility coefficient K gives the second derivative,

$$C''_\sigma = \frac{2}{n_{\text{sat}} \left(n_{\text{sat}}^{(s)}\right)^2} \left[\frac{1}{3} (\mu_{\text{sat}}^* - M_{\text{sat}}^* g_{\text{sat}}) - \frac{K}{9} + \left(C_\omega + 2C'_\omega n_{\text{sat}} + \frac{1}{2} C''_\omega n_{\text{sat}}^2 \right) n_{\text{sat}} - (C_\sigma + C'_\sigma n_{\text{sat}}) n_{\text{sat}}^{(s)} g_{\text{sat}} - C'_\sigma \left(n_{\text{sat}}^{(s)}\right)^2 \right], \quad (\text{A15})$$

for the σ meson.

7. The symmetry energy at saturation J is used to calculate the coupling of the ρ meson at saturation,

$$\Gamma_\rho^{(0)} = \sqrt{C_\rho} M_\rho, \quad (\text{A16})$$

where

$$C_\rho = \frac{2}{n_{\text{sat}}} \left[J - \frac{(k_{\text{sat}}^*)^2}{6\mu_{\text{sat}}^*} \right]. \quad (\text{A17})$$

8. The slope parameter L of the symmetry energy at saturation gives the derivative

$$C'_\rho = \frac{2}{3n_{\text{sat}}^2} \left\{ L - 3J - \frac{(k_{\text{sat}}^*)^2}{3\mu_{\text{sat}}^*} \left[\frac{1}{2} \left(\frac{M_{\text{sat}}^*}{\mu_{\text{sat}}^*} \right)^2 \left(1 - 3 \frac{n_{\text{sat}}}{M_{\text{sat}}^*} h_{\text{sat}} \right) - 1 \right] \right\}, \quad (\text{A18})$$

for the ρ meson at saturation. Then the parameter

$$a_\rho = -\frac{1}{2} \frac{C'_\rho}{C_\rho} n_{\text{sat}}, \quad (\text{A19})$$

in the function $f_\rho(x)$ is found.

9. The values of C_j and their derivatives determine the couplings and first derivatives

$$\Gamma_j^{(0)} = \sqrt{C_j} M_j, \quad \text{and} \quad \Gamma_j' = \frac{1}{2} \Gamma_j^{(0)} \frac{C_j'}{C_j}, \quad (\text{A20})$$

as well as the second derivatives

$$\Gamma_j'' = \frac{1}{2} \Gamma_j^{(0)} \left[\frac{C_j''}{C_j} - \frac{1}{2} \left(\frac{C_j'}{C_j} \right)^2 \right], \quad (\text{A21})$$

for $j = \sigma$ and ω . Then also the derivatives

$$f_j'(1) = \frac{\Gamma_j'}{\Gamma_j^{(0)}}, \quad \text{and} \quad f_j''(1) = \frac{\Gamma_j''}{\Gamma_j^{(0)}}, \quad (\text{A22})$$

of the functions $f_j(x)$ are known.

10. Finally, the parameters of the rational functions $f_j(x)$ for the isoscalar mesons can be found with help of the explicit expressions;

$$f_j'(x) = 2a_j(b_j - c_j) \frac{x + d_j}{[1 + c_j(x + d_j)^2]^2}, \quad (\text{A23})$$

$$f_j''(x) = 2a_j(b_j - c_j) \frac{1 - 3c(x + d_j)^2}{[1 + c_j(x + d_j)^2]^3}, \quad (\text{A24})$$

for the first and second derivatives of the functions $f_j(x)$. The ratio,

$$r_{21} = \frac{f_\omega''(1)}{f_\omega(1)} = \frac{d_j^2 - (1 + d_j)^2}{[d_j^2 + (1 + d_j)^2/3](1 + d_j)}, \quad (\text{A25})$$

is a function of d_j only because of the constraint $1 = 3c_j d_j^2$ that follows from $f_j''(0) = 0$. Thus the value of d_j can be obtained by a simple numerical search or iteration. Then $c_j = 1/(3d_j^2)$ is known as well and b_j is calculated from

$$b_j = \frac{c_j z + r_{10}}{z - (1 + d_j)^2 r_{10}}, \quad (\text{A26})$$

with the auxiliary quantity

$$z = \frac{2(1 + d_j)}{1 + c_j(1 + d_j)^2}. \quad (\text{A27})$$

Finally, the normalization condition $f_j(1) = 1$ gives

$$a_j = \frac{1 + c_j(1 + d_j)^2}{1 + b_j(1 + d_j)^2}. \quad (\text{A28})$$

References

- [1] B.K. Agrawal, S. Shlomo, V.K. Au, Determination of the parameters of a Skyrme type effective interaction using the simulated annealing approach. *Phys. Rev. C* **72**, 014310 (2005). <https://doi.org/10.1103/PhysRevC.72.014310>. [arXiv:nucl-th/0505071](https://arxiv.org/abs/nucl-th/0505071)
- [2] J.R. Stone, P.G. Reinhard, The Skyrme Interaction in finite nuclei and nuclear matter. *Prog. Part. Nucl. Phys.* **58**, 587–657 (2007). <https://doi.org/10.1016/j.ppnp.2006.07.001>. [arXiv:nucl-th/0607002](https://arxiv.org/abs/nucl-th/0607002)
- [3] M. Dutra, O. Lourenco, J.S. Sa Martins, A. Delfino, J.R. Stone, P.D. Stevenson, Skyrme Interaction and Nuclear Matter Constraints. *Phys. Rev. C* **85**, 035201 (2012). <https://doi.org/10.1103/PhysRevC.85.035201>. [arXiv:1202.3902](https://arxiv.org/abs/1202.3902) [nucl-th]
- [4] R. Sellahewa, A. Rios, Isovector properties of the Gogny interaction. *Phys. Rev. C* **90**(5), 054327 (2014). <https://doi.org/10.1103/PhysRevC.90.054327>. [arXiv:1407.8138](https://arxiv.org/abs/1407.8138) [nucl-th]
- [5] P.G. Reinhard, M. Rufa, J. Maruhn, W. Greiner, J. Friedrich, Nuclear Ground State Properties in a Relativistic Meson Field Theory. *Z. Phys. A* **323**, 13–25 (1986)
- [6] M. Rufa, P.G. Reinhard, J.A. Maruhn, W. Greiner, M.R. Strayer, Optimal parametrization for the relativistic mean-field model of the nucleus. *Phys. Rev. C* **38**, 390–409 (1988). <https://doi.org/10.1103/PhysRevC.38.390>

- [7] P.G. Reinhard, The Relativistic Mean Field Description of Nuclei and Nuclear Dynamics. Rept. Prog. Phys. **52**, 439 (1989). <https://doi.org/10.1088/0034-4885/52/4/002>
- [8] B.D. Serot, Quantum hadrodynamics. Rept. Prog. Phys. **55**, 1855–1946 (1992). <https://doi.org/10.1088/0034-4885/55/11/001>
- [9] C. Fuchs, H. Lenske, H.H. Wolter, Density dependent hadron field theory. Phys. Rev. C **52**, 3043–3060 (1995). <https://doi.org/10.1103/PhysRevC.52.3043>. [arXiv:nucl-th/9507044](https://arxiv.org/abs/nucl-th/9507044)
- [10] P. Ring, Relativistic mean field in finite nuclei. Prog. Part. Nucl. Phys. **37**, 193–263 (1996). [https://doi.org/10.1016/0146-6410\(96\)00054-3](https://doi.org/10.1016/0146-6410(96)00054-3)
- [11] S. Typel, H.H. Wolter, Relativistic mean field calculations with density dependent meson nucleon coupling. Nucl. Phys. A **656**, 331–364 (1999). [https://doi.org/10.1016/S0375-9474\(99\)00310-3](https://doi.org/10.1016/S0375-9474(99)00310-3)
- [12] D. Vretenar, A.V. Afanasjev, G.A. Lalazissis, P. Ring, Relativistic Hartree Bogoliubov theory: static and dynamic aspects of exotic nuclear structure. Phys. Rept. **409**, 101–259 (2005). <https://doi.org/10.1016/j.physrep.2004.10.001>
- [13] J. Meng, H. Toki, S.G. Zhou, S.Q. Zhang, W.H. Long, L.S. Geng, Relativistic Continuum Hartree Bogoliubov theory for ground state properties of exotic nuclei. Prog. Part. Nucl. Phys. **57**, 470–563 (2006). <https://doi.org/10.1016/j.ppnp.2005.06.001>. [arXiv:nucl-th/0508020](https://arxiv.org/abs/nucl-th/0508020)
- [14] T. Niksic, D. Vretenar, P. Ring, Relativistic Nuclear Energy Density Functionals: Mean-Field and Beyond. Prog. Part. Nucl. Phys. **66**, 519–548 (2011). <https://doi.org/10.1016/j.ppnp.2011.01.055>. [arXiv:1102.4193](https://arxiv.org/abs/1102.4193) [nucl-th]
- [15] M. Dutra, O. Lourenço, S.S. Avancini, B.V. Carlson, A. Delfino, D.P. Menezes, C. Providência, S. Typel, J.R. Stone, Relativistic Mean-Field Hadronic Models under Nuclear Matter Constraints. Phys. Rev. C **90**(5), 055203 (2014). <https://doi.org/10.1103/PhysRevC.90.055203>. [arXiv:1405.3633](https://arxiv.org/abs/1405.3633) [nucl-th]
- [16] J.D. Walecka, A Theory of highly condensed matter. Annals Phys. **83**, 491–529 (1974). [https://doi.org/10.1016/0003-4916\(74\)90208-5](https://doi.org/10.1016/0003-4916(74)90208-5)
- [17] W.H. Long, H. Sagawa, N. Van Giai, J. Meng, Shell Structure and rho-Tensor Correlations in Density-Dependent Relativistic Hartree-Fock theory. Phys. Rev. C **76**, 034314 (2007). <https://doi.org/10.1103/PhysRevC.76.034314>. [arXiv:0706.3497](https://arxiv.org/abs/0706.3497) [nucl-th]

- [18] S. Typel, D. Alvear Terrero, Parametrisations of relativistic energy density functionals with tensor couplings. *Eur. Phys. J. A* **56**(6), 160 (2020). <https://doi.org/10.1140/epja/s10050-020-00172-2>. arXiv:2003.02085 [nucl-th]
- [19] M. Salinas, J. Piekarewicz, Impact of tensor couplings with scalar mixing on covariant energy density functionals. *Phys. Rev. C* **109**(4), 045807 (2024). <https://doi.org/10.1103/PhysRevC.109.045807>. arXiv:2312.13474 [nucl-th]
- [20] S. Typel, Lagrange-Mesh Method for Deformed Nuclei With Relativistic Energy Density Functionals. *Front. in Phys.* **6**, 73 (2018). <https://doi.org/10.3389/fphy.2018.00073>
- [21] N.M. Hugenholtz, L. van Hove, A theorem on the single particle energy in a Fermi gas with interaction. *Physica* **24**, 363–376 (1958). [https://doi.org/10.1016/S0031-8914\(58\)95281-9](https://doi.org/10.1016/S0031-8914(58)95281-9)
- [22] G.G. Simon, C. Schmitt, F. Borkowski, V.H. Walther, Absolute electron Proton Cross-Sections at Low Momentum Transfer Measured with a High Pressure Gas Target System. *Nucl. Phys. A* **333**, 381–391 (1980). [https://doi.org/10.1016/0375-9474\(80\)90104-9](https://doi.org/10.1016/0375-9474(80)90104-9)
- [23] M. Wang, W.J. Huang, F.G. Kondev, G. Audi, S. Naimi, The AME 2020 atomic mass evaluation (II). Tables, graphs and references. *Chin. Phys. C* **45**(3), 030003 (2021). <https://doi.org/10.1088/1674-1137/abddaf>
- [24] H. De Vries, C.W. De Jager, C. De Vries, Nuclear charge and magnetization density distribution parameters from elastic electron scattering. *Atom. Data Nucl. Data Tabl.* **36**, 495–536 (1987). [https://doi.org/10.1016/0092-640X\(87\)90013-1](https://doi.org/10.1016/0092-640X(87)90013-1)
- [25] G. Fricke, C. Bernhardt, K. Heilig, L.A. Schaller, L. Schellenberg, E.B. Shera, C.W. de Jager, Nuclear Ground State Charge Radii from Electromagnetic Interactions. *Atom. Data Nucl. Data Tabl.* **60**, 177–285 (1995). <https://doi.org/10.1006/adnd.1995.1007>
- [26] E.G. Nadjakov, K.P. Marinova, Y.P. Gangrsky, Systematics of Nuclear Charge Radii. *Atom. Data Nucl. Data Tabl.* **56**, 133–157 (1994). <https://doi.org/10.1006/adnd.1994.1004>
- [27] I. Angeli, K.P. Marinova, Table of experimental nuclear ground state charge radii: An update. *Atom. Data Nucl. Data Tabl.* **99**(1), 69–95 (2013). <https://doi.org/10.1016/j.adt.2011.12.006>
- [28] N. Kalantar-Nayestanaki, et al., Magnetic structure of ^{17}O at high momentum. *Phys. Rev. Lett.* **60**, 1707–1710 (1988). <https://doi.org/10.1103/PhysRevLett.60.1707>

- [29] S. Platchkov, A. Amroun, P. Bricault, J.M. Cavedon, P.K.A. de Witt Huberts, P. Dreux, B. Frois, C.D. Goodman, D. Goutte, J. Martino, V. Meot, G.A. Peterson, X.H. Phan, S. Raman, I. Sick, Measurement of the $1f_{7/2}$ -neutron-orbit radius in ^{41}Ca . Phys. Rev. Lett. **61**, 1465–1468 (1988). <https://doi.org/10.1103/PhysRevLett.61.1465>. URL <https://link.aps.org/doi/10.1103/PhysRevLett.61.1465>
- [30] B.N.L. National Nuclear Data Center. Evaluated nuclear structure data files. URL <https://www.nndc.bnl.gov/ensdf/>
- [31] S. Typel, Relativistic model for nuclear matter and atomic nuclei with momentum-dependent self-energies. Phys. Rev. C **71**, 064301 (2005). <https://doi.org/10.1103/PhysRevC.71.064301>. [arXiv:nucl-th/0501056](https://arxiv.org/abs/nucl-th/0501056)
- [32] D.H. Youngblood, H.L. Clark, Y.W. Lui, Incompressibility of Nuclear Matter from the Giant Monopole Resonance. Phys. Rev. Lett. **82**, 691–694 (1999). <https://doi.org/10.1103/PhysRevLett.82.691>
- [33] W.H. Press, B.P. Flannery, S.A. Teukolsky, W.T. Vetterling, *Numerical recipes - the art of scientific computing* (Cambridge University Press, Cambridge, 1986)
- [34] S. Typel, G. Röpke, T. Klähn, D. Blaschke, H.H. Wolter, Composition and thermodynamics of nuclear matter with light clusters. Phys. Rev. C **81**, 015803 (2010). <https://doi.org/10.1103/PhysRevC.81.015803>. [arXiv:0908.2344](https://arxiv.org/abs/0908.2344) [nucl-th]
- [35] J.C. Slater, A Simplification of the Hartree-Fock Method. Phys. Rev. **81**, 385 (1951). <https://doi.org/10.1103/PhysRev.81.385>
- [36] J.A. Nolen, Jr., J.P. Schiffer, Coulomb energies. Ann. Rev. Nucl. Part. Sci. **19**, 471–526 (1969). <https://doi.org/10.1146/annurev.ns.19.120169.002351>
- [37] S. Shlomo, W.G. Love, Core Polarization and Coulomb Displacement Energies. Phys. Scr. **26**, 280 (1982). <https://doi.org/10.1088/0031-8949/26/4/005>
- [38] D. Adhikari, et al., Precision Determination of the Neutral Weak Form Factor of ^{48}Ca . Phys. Rev. Lett. **129**(4), 042501 (2022). <https://doi.org/10.1103/PhysRevLett.129.042501>. [arXiv:2205.11593](https://arxiv.org/abs/2205.11593) [nucl-ex]
- [39] D. Adhikari, et al., Accurate Determination of the Neutron Skin Thickness of ^{208}Pb through Parity-Violation in Electron Scattering. Phys. Rev. Lett. **126**(17), 172502 (2021).

- <https://doi.org/10.1103/PhysRevLett.126.172502>. [arXiv:2102.10767](https://arxiv.org/abs/2102.10767) [nucl-ex]
- [40] S. Shlomo, R. Schaeffer, The difference between neutron and proton radii in the Ca isotopes. *Phys. Lett. B* **83**, 5–8 (1979). [https://doi.org/10.1016/0370-2693\(79\)90875-X](https://doi.org/10.1016/0370-2693(79)90875-X)
- [41] B.C. Clark, L.J. Kerr, S. Hama, Neutron densities from a global analysis of medium-energy proton nucleus elastic scattering. *Phys. Rev. C* **67**, 054605 (2003). <https://doi.org/10.1103/PhysRevC.67.054605>. [arXiv:nucl-th/0209052](https://arxiv.org/abs/nucl-th/0209052)
- [42] K. Chatziioannou, H.T. Cromartie, S. Gandolfi, I. Tews, D. Radice, A.W. Steiner, A.L. Watts, Neutron stars and the dense matter equation of state: from microscopic theory to macroscopic observations (2024). [arXiv:2407.11153](https://arxiv.org/abs/2407.11153) [nucl-th]
- [43] I. Tews, R. Somasundaram, D. Lonardoni, H. Götting, R. Seutin, J. Carlson, S. Gandolfi, K. Hebeler, A. Schwenk, Neutron matter from local chiral EFT interactions at large cutoffs (2024). [arXiv:2407.08979](https://arxiv.org/abs/2407.08979) [nucl-th]
- [44] W.G. Lynch, M.B. Tsang, Decoding the density dependence of the nuclear symmetry energy. *Phys. Lett. B* **830**, 137098 (2022). <https://doi.org/10.1016/j.physletb.2022.137098>. [arXiv:2106.10119](https://arxiv.org/abs/2106.10119) [nucl-th]
- [45] C.Y. Tsang, M.B. Tsang, W.G. Lynch, R. Kumar, C.J. Horowitz, Determination of the equation of state from nuclear experiments and neutron star observations. *Nature Astron.* **8**(3), 328–336 (2024). <https://doi.org/10.1038/s41550-023-02161-z>. [arXiv:2310.11588](https://arxiv.org/abs/2310.11588) [nucl-th]
- [46] I. Vidana, C. Providencia, A. Polls, A. Rios, Density dependence of the nuclear symmetry energy: A Microscopic perspective. *Phys. Rev. C* **80**, 045806 (2009). <https://doi.org/10.1103/PhysRevC.80.045806>. [arXiv:0907.1165](https://arxiv.org/abs/0907.1165) [nucl-th]
- [47] M. Falanga, E. Bozzo, A. Lutovinov, J.M. Bonnet-Bidaud, Y. Fetisova, J. Puls, Ephemeris, orbital decay, and masses of ten eclipsing high-mass X-ray binaries. *Astron. Astrophys.* **577**, A130 (2015). <https://doi.org/10.1051/0004-6361/201425191>. [arXiv:1502.07126](https://arxiv.org/abs/1502.07126) [astro-ph.HE]
- [48] J. Antoniadis, et al., A Massive Pulsar in a Compact Relativistic Binary. *Science* **340**, 6131 (2013). <https://doi.org/10.1126/science.1233232>. [arXiv:1304.6875](https://arxiv.org/abs/1304.6875) [astro-ph.HE]
- [49] E. Fonseca, et al., The NANOGrav Nine-year Data Set: Mass and Geometric Measurements of Binary Millisecond Pulsars. *Astrophys. J.* **832**(2), 167 (2016). <https://doi.org/10.3847/0004-637X/832/2/167>. [arXiv:1603.00545](https://arxiv.org/abs/1603.00545) [astro-ph.HE]

- [50] M.C. Miller, et al., PSR J0030+0451 Mass and Radius from *NICER* Data and Implications for the Properties of Neutron Star Matter. *Astrophys. J. Lett.* **887**(1), L24 (2019). <https://doi.org/10.3847/2041-8213/ab50c5>. [arXiv:1912.05705](https://arxiv.org/abs/1912.05705) [astro-ph.HE]
- [51] T.E. Riley, et al., A *NICER* View of PSR J0030+0451: Millisecond Pulsar Parameter Estimation. *Astrophys. J. Lett.* **887**(1), L21 (2019). <https://doi.org/10.3847/2041-8213/ab481c>. [arXiv:1912.05702](https://arxiv.org/abs/1912.05702) [astro-ph.HE]
- [52] M.C. Miller, et al., The Radius of PSR J0740+6620 from *NICER* and *XMM-Newton* Data. *Astrophys. J. Lett.* **918**(2), L28 (2021). <https://doi.org/10.3847/2041-8213/ac089b>. [arXiv:2105.06979](https://arxiv.org/abs/2105.06979) [astro-ph.HE]
- [53] T.E. Riley, et al., A *NICER* View of the Massive Pulsar PSR J0740+6620 Informed by Radio Timing and *XMM-Newton* Spectroscopy. *Astrophys. J. Lett.* **918**(2), L27 (2021). <https://doi.org/10.3847/2041-8213/ac0a81>. [arXiv:2105.06980](https://arxiv.org/abs/2105.06980) [astro-ph.HE]
- [54] R.C. Tolman, Static solutions of Einstein's field equations for spheres of fluid. *Phys. Rev.* **55**, 364–373 (1939). <https://doi.org/10.1103/PhysRev.55.364>
- [55] J.R. Oppenheimer, G.M. Volkoff, On massive neutron cores. *Phys. Rev.* **55**, 374–381 (1939). <https://doi.org/10.1103/PhysRev.55.374>
- [56] J. Duflo, A.P. Zuker, Microscopic mass formulae. *Phys. Rev. C* **52**, R23 (1995). <https://doi.org/10.1103/PhysRevC.52.R23>. [arXiv:nuc1-th/9505011](https://arxiv.org/abs/nuc1-th/9505011)
- [57] M. Oertel, M. Hempel, T. Klöhn, S. Typel, Equations of state for supernovae and compact stars. *Rev. Mod. Phys.* **89**(1), 015007 (2017). <https://doi.org/10.1103/RevModPhys.89.015007>. [arXiv:1610.03361](https://arxiv.org/abs/1610.03361) [astro-ph.HE]
- [58] S. Typel, Equations of state for astrophysical simulations from generalized relativistic density functionals. *J. Phys. G* **45**(11), 114001 (2018). <https://doi.org/10.1088/1361-6471/aadea5>
- [59] J.R. Stone, V. Dexheimer, P.A.M. Guichon, A.W. Thomas, S. Typel, Equation of state of hot dense hyperonic matter in the Quark–Meson-Coupling (QMC-A) model. *Mon. Not. Roy. Astron. Soc.* **502**(3), 3476–3490 (2021). <https://doi.org/10.1093/mnras/staa4006>. [arXiv:1906.11100](https://arxiv.org/abs/1906.11100) [nucl-th]